LA-UR-96-4703

CONF-960702--1

Title:

# Analysis and Design Methodology for the Development of Optimized, Direct-Dectection $CO_2$ DIAL Receivers.

Author(s):
Bradly J. Cooke, LANL
Bryan E. Laubscher, LANL
Maureen Cafferty, LANL
Nicholas L. Olivas, LANL
Mark J. Schmitt, LANL
Kenneth R. Fuller, LANL
Roy M. Goeller, LANL
Donald E. Mietz, LANL
Joe J. Tiee, LANL
Robert K. Sander, LANL
John L. Vampola, SBRC
Stephen L. Price, SBRC
Ichiro Kasai, SBRC

Submitted to:
SPIE
1997 San Diego
Infrared Instrumentation

**Los Alamos**
NATIONAL LABORATORY

# Analysis and Design Methodology for the Development of Optimized, Direct-Detection $CO_2$ DIAL Receivers

Bradly J. Cooke, Bryan E. Laubscher, Maureen Cafferty, Nicholas L. Olivas, Mark J. Schmitt,
Kenneth R. Fuller, Roy M. Goeller, Donald E. Mietz, Joe J. Tiee and Robert K. Sander

Los Alamos National Laboratory
MS - D448, P.O. Box 1663
Los Alamos, New Mexico 87545

John L. Vampola, Stephen L. Price and Ichiro Kasai

Santa Barbara Research Center
75 Coromar Dr.
Goleta, California 93117

## ABSTRACT

The analysis methodology and corresponding analytical tools for the design of optimized, low-noise, hard target return $CO_2$ Differential Absorption Lidar (DIAL) receiver systems implementing both single element detectors and multi-pixel imaging arrays for passive/active, remote-sensing applications are presented. System parameters and components composing the receiver include: aperture, focal length, field of view, cold shield requirements, image plane dimensions, pixel dimensions, pixel pitch and fill factor, detection quantum efficiency, optical filter requirements, amplifier and temporal sampling parameters. The performance analysis is accomplished by calculating the system's $CO_2$ laser range response, total noise, optical geometric form factor and optical resolution. The noise components include speckle, photon noise due to signal, scene and atmospheric background, cold shield, and electronic noise. System resolution is simulated through cascaded optical transfer functions and includes effects due to atmosphere, optics, image sampling, and system motion.

Experimental results of a developmental single-element detector receiver designed to detect 100 ns wide laser pulses (10-100 kHz pulse repetition rates) backscattered from hard-targets at nominal ranges of 10 km are presented. The receiver sensitivity is near-background noise limited, given an 8.5-11.5 μm radiant optical bandwidth, with the total noise floor spectrally white for maximum pulse averaging efficiency.

Keywords: $CO_2$ Lidar/Dial receiver, passive/active remote sensing, correlated noise

## 1. INTRODUCTION

The basic function of an infrared (IR) $CO_2$ Differential Absorption LIDAR/LADAR (DIAL) receiver is the optical collection, electro-optical conversion, electronic processing and display of hard target reflected or scattered IR electromagnetic energy. The major functions associated with a typical DIAL system are shown in **Figure 1**[1]. IR radiation from a $CO_2$ laser propagates through the atmosphere, scatters from the target, back propagates through the atmosphere, is mapped onto an image plane through collection optics, then sampled and converted into electronic signals for processing and display. The basic measurement performed is a measure of the magnitude of the returned optical power or energy at a given laser line. The logarithmic difference of two or more laser lines provides the differential absorption information between the sampled wavelengths. The actual configuration and implementation of a given DIAL system depends strongly on the requirements and system specifications. For what immediately follows and throughout the remainder of this paper, the term *Signal*, will always represent the desired physical measurement with the quality of the measure given by the signal-to-noise ratio (SNR)[2]

$$SNR = \frac{Signal}{\sigma_{system}} , \qquad (1)$$

where *Signal* is the mean signal value and $\sigma_{system}$ is the signal standard deviation due to system noise. The composition of system noise and how it is calculated is addressed later in the paper. The objective of this paper is to introduce the fundamental optical resolution and noise processes specific to DIAL systems and apply them to the development and design of optimal receivers. The analytic tools employed in analyzing the receiver optical resolution and noise processes are described in **Section 2**. **Section 3** presents the experimental results for a prototype 10 km range DIAL receiver where the tools of **Section 2** are applied to optimize the receiver performance, maximizing the SNR of **Equation 1**.

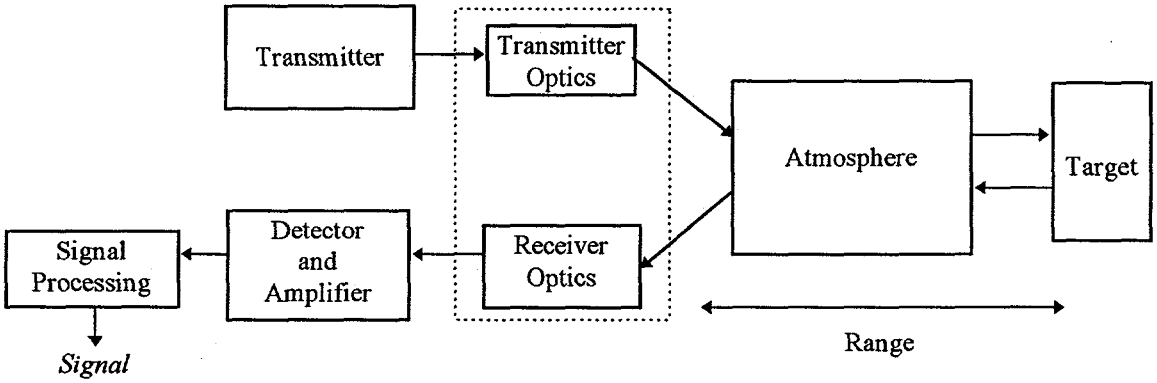

**Figure 1.** Simplified DIAL System Signal Chain.

## 2. RECEIVER ANALYSIS TOOLS

The receiver analysis, diagrammed in **Figure 2**, divides the problem into two parts: i) receiver resolution and Geometric Form Factor (GFF) modulation and ii) signal detection. GFF and resolution quantifies the efficiency in transmission of spatial information from the target through electronic capture, while signal detection evaluates detection efficiency in the presence of noise. The two components can be combined to generate performance parameters for a given target.

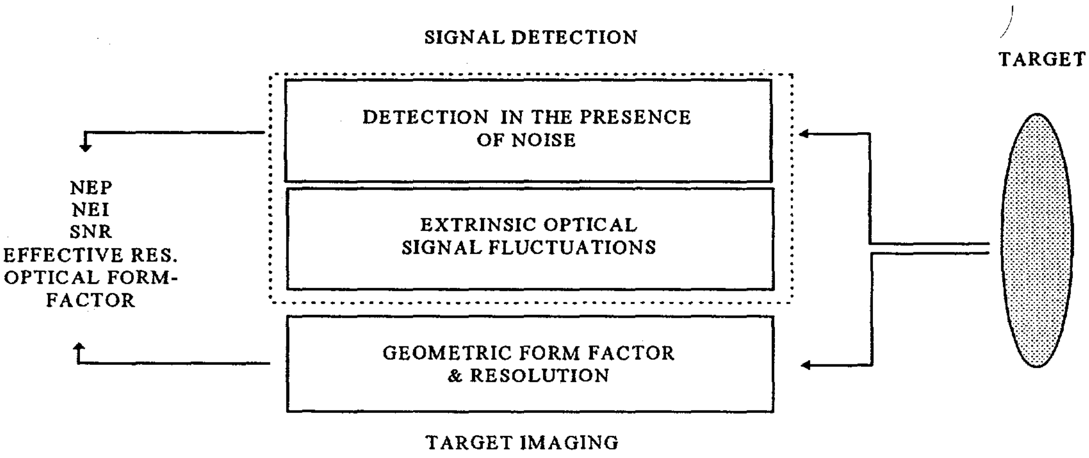

**Figure 2.** Receiver Analysis Approach.

### 2.1. Transmitter/Receiver Optical Geometric Form Factor and Receiver Resolution

#### 2.1.A. Geometric form factor

The geometric form factor[3, 4, 5] (GFF) is the ratio of the transmitted laser beam's optical intensity distribution spatially integrated over the receiver's active detection field-of-view (FOV) to the total integrated laser optical intensity distribution. Both the laser intensity distribution and receiver FOV are referenced at the target. Throughout the remainder of this paper, the laser beam's spatial profile will be assumed Gaussian ($TEM_{oo}$) for simplicity and clarity (where appropriate, the equations in this section can be adapted for non-Gaussian profiles in a straight-forward manner). In addition, the receiver's active detection area will refer either to single or multiple detector elements (focal plane array pixels) in the image plane. Ideally, the entire transmitted intensity distribution is captured by the active detection area leading to a 100% form factor. However, mechanisms including transmitter beam and receiver FOV overlap, receiver obstruction for coaxial systems, transmitter/receiver separation of biaxial systems, and transmitter/receiver line-of -sight (LOS) alignment error effectively degrade the form factor.

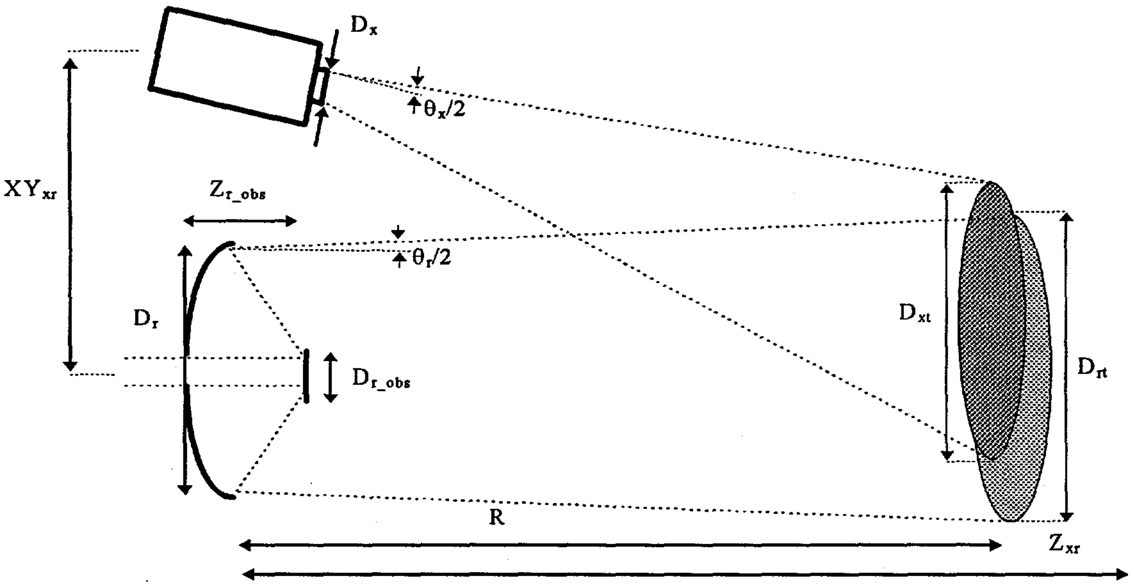

**Figure 3.** Transmitter/Receiver Optical Parameters.

Referring to the transmitter/receiver parameters of **Figure 3**, the geometric form factor at range $R$ is evaluated by integrating over the normalized transmitted beam and receiver FOV overlap area (the area over which the shaded disks intersect in **Figure 3**),

$$\xi_{xr}(R) = \frac{2}{\pi\,\omega_{xt}(R)^2} \iint_{D_{rt}(R)} I_{xr}(R,x,y)\,dx\,dy\,. \tag{2}$$

Where

$$D_{rt}(R) = D_r + 2\,R\,\tan\!\left(\frac{\theta_r}{2}\right) \tag{3}$$

is the receiver FOV at the target (at range R),

$$\omega_{xt}(R) = \frac{D_{xt}(R)}{\alpha} = \frac{2}{\alpha}\sqrt{\frac{D_x^2}{4}\left(1+2\,\frac{R}{D_x}\,\tan\!\left(\frac{\theta_x}{2}\right)\right)^2 + \left(\frac{\lambda_o\,R}{\pi\,\rho_o(R)}\right)^2} \tag{4}$$

is the beam spotsize at the target, with $\alpha$ relating the effective beam diameter to the Gaussian beam waist ($\alpha = \sqrt{2}$ for a 1/e clipped beam system), $\lambda_o$ is the laser center wavelength and $\rho_o$ the laser beam's effective transverse coherence length at range $R$. The last term in **Equation 4** accounts for beam expansion and wander due to atmospheric turbulence. Finally, the transmitter/receiver overlap intensity at range $R$ is

$$I_{xr}(R,x,y) = \begin{cases} 0 \quad if & \left( \begin{array}{c} \sqrt{x^2+y^2} > \dfrac{D_{rt}(R)}{2} \\ or \\ \sqrt{\left(\dfrac{R-Z_{r\_obs}}{R}x\right)^2 + \left(\dfrac{R-Z_{r\_obs}}{R}\left(y - R\tan(\zeta) - \left(XY_{xr} - R\tan^{-1}\left(\dfrac{XY_{xr}}{Z_{xr}}\right)\right)\right)\right)^2} < \dfrac{D_{r\_obs}}{2} \end{array} \right) \\ e^{-\left(2\dfrac{x^2+\left(y-R\tan(\zeta)-\left(XY_{xr}-R\tan^{-1}\left(\frac{XY_{xr}}{Z_{xr}}\right)\right)\right)^2}{\omega_{xt}(R)^2}\right)} & otherwise, \end{cases} \tag{5}$$

with $\zeta$ the LOS pointing error angle [rad] and $Z_{xr}$ the transmitter/receiver convergence range which applies only to biaxial systems.

## 2.2.B. Optical resolution

The image chain shown in **Figure 4** is a schematic description of the primary optical elements from target image to output. The image forming process depicted in **Figure 4** must account for loss of transmission fidelity as a function of spatial frequency or spatial resolution. This degradation in fidelity is due to the aggregate degradation of the individual components shown in the boxes of **Figure 4**, and can be quantified by either a system optical transfer function (OTF) or by a point spread function (PSF), both of which are described in two dimensions. The final image captured by the transmission process is obtained by taking the convolution of the system PSF with the original object space image or multiplying the system OTF by the Fourier transform (FT) of the original input image and then inverse Fourier transforming (IFT) this product to obtain a final image. Note, it has been implicitly assumed that the system is linear and that the system OTF and PSF form a Fourier transform pair. For a given input scene defined at center wavelength, $\lambda_o$, the output target image is[6, 7]:

Spatial Domain: $$\Phi_{image}(x,y,\lambda_o) = PSF_{sys}(x,y,\lambda_o) * \Phi_{target}(x,y,\lambda_o) \tag{6}$$

Frequency Domain: $$\Phi_{image}(x,y,\lambda_o) = IFT\{OTF_{sys}(k_x,k_y,\lambda_o) \cdot FT[\Phi_{target}(x,y,\lambda_o)]\} \tag{7}$$

where $k_x$ and $k_y$ [cycles/m] are the spatial frequency domain coordinates and the system OTF is evaluated as the product of the components in **Figure 4**,

$$\begin{aligned} OTF_{sys}(k_x,k_y,\lambda_o) = {} & OTF_{sp}(k_x,k_y,\lambda_o) \cdot OTF_{sa}(k_x,k_y,\lambda_o) \cdot OTF_{ta}(k_x,k_y,\lambda_o) \cdot OTF_{rv}(k_x,k_y,\lambda_o) \cdot \\ & OTF_{df}(k_x,k_y,\lambda_o) \cdot OTF_{ab}(k_x,k_y,\lambda_o) \cdot OTF_{ap}(k_x,k_y,\lambda_o) \cdot OTF_{atm}(k_x,k_y,\lambda_o). \end{aligned} \tag{8}$$

It should be stated that **Equation 8** depicts an *incoherent* representation of the optical system, which is appropriate for the *passive* aspects of remote sensing. However, for *active* remote sensing, **Equation 8** should be considered an approximation of what is, strictly speaking, a *coherent* or *partially-coherent* system.[8] The approximation appears valid based on our coherent/incoherent analysis of a simple circular aperture system - primarily because return pulse magnitude (power), instead of amplitude and phase, is detected in DIAL (the effects of hard-target speckle will be discussed is **Section 2.2.A.**). A good tutorial on coherent and partial coherent imaging is given in *Tutorials in Fourier Optics*.[9]

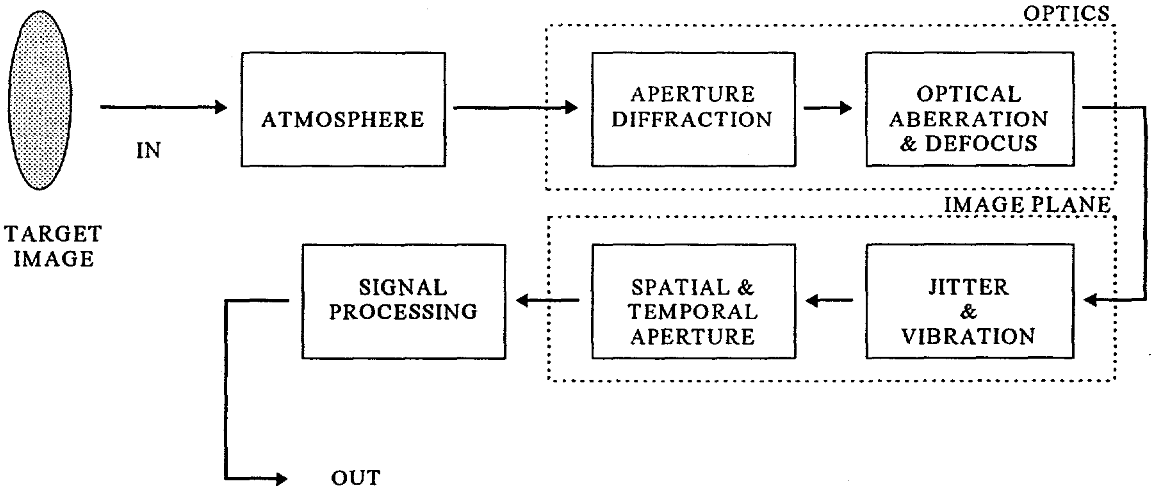

**Figure 4.** Imaging System.

In practice, the degradation components described in **Figure 4** are expressed analytically as component OTF's. Closed form mathematical models of these OTF's are available whereas the corresponding component PSF models tend to be mathematically intractable and are generally not available. **Section 2.1.C** lists a set of OTF's useful for analyzing the system components of **Figure 4**. Refer to **Figure 3** for receiver aperture parameters.

### 2.1.C. Optical transfer functions

Atmospheric: The optical transfer function for atmospheric turbulence is approximated by [10, 11, 12]

$$OTF_{atm}(k_r,\lambda)=e^{-3.44\left(\frac{1}{2\pi}\frac{\lambda f_l k_r}{\frac{\rho_o}{2.1}}\right)^{\frac{5}{3}}}, \tag{9}$$

with the weak-turbulence atmospheric optical transverse coherence length (in meters) approximated by

$$\rho_o(\lambda)=\begin{cases}\left[1.46\left(\frac{2\pi}{\lambda}\right)\int_0^R C_n^2\left(h_o+\left|r\sin(\theta_s)\right|\right)\left(\frac{r}{R}\right)^{\frac{5}{3}}dr\right]^{-\frac{3}{5}} & \theta_s\le 0\\ \left[1.46\left(\frac{2\pi}{\lambda}\right)\int_0^R C_n^2\left(h_o+\left|r\sin(\theta_s)\right|\right)\left(1-\frac{r}{R}\right)^{\frac{5}{3}}dr\right]^{-\frac{3}{5}} & \textit{otherwise,}\end{cases} \tag{10}$$

where,

$f_l$ = effective focal length [m],
$\theta_s$ = slant angle ($\theta_s$ looking *up* through atmosphere, $-\theta_s$ looking *down* through atmosphere) [rad],
$h_o$ = initial aperture or target height (lower of the two) [m],
$R$ = aperture to target range [m],
$C_n^2$ = atmospheric refractive index structure factor [$m^{-2/3}$],
$k_r=\sqrt{k_x^2+k_y^2}$ = spatial frequency [cycles/m].

Annular Aperture (O'Neill model):[13] For annular aperture of diameter $D_r$, a radial obstruction of diameter $D_{r\_obs}$, and focal length $f_l$,

$$OTF_{ap}(k_r,\lambda)=\frac{I_1(k_r,\lambda)+I_2(k_r,\lambda)+I_3(k_r,\lambda)}{1-\left(\frac{D_{r\_obs}}{D_r}\right)^2} \tag{11}$$

where:

$$I_1(k_r,\lambda)=\begin{cases}\frac{2}{\pi}\left[\cos^{-1}\left(\frac{\lambda\, f_l\, k_r}{D_r}\right)-\frac{\lambda\, f_l\, k_r}{D_r}\sqrt{1-\left(\frac{\lambda\, f_l\, k_r}{D_r}\right)^2}\right], & 0\le k_r\le\frac{D_r}{\lambda\, f_l}\\ 0, \quad k_r>\frac{D_r}{\lambda\, f_l} & \end{cases} \tag{12}$$

$$I_2(k_r,\lambda)=\begin{cases}\frac{2}{\pi}\left(\frac{D_{r\_obs}}{D_r}\right)^2\left[\cos^{-1}\left(\frac{\lambda\, f_l\, k_r}{D_{r\_obs}}\right)-\frac{\lambda\, f_l\, k_r}{D_{r\_obs}}\sqrt{1-\left(\frac{\lambda\, f_l\, k_r}{D_{r\_obs}}\right)^2}\right], & 0\le k_r\le\frac{D_{r\_obs}}{\lambda\, f_l}\\ 0, \quad k_r>\frac{D_{r\_obs}}{\lambda\, f_l} & \end{cases}$$

$$I_3(k_r,\lambda)=\begin{cases}-2\left(\frac{D_{r\_obs}}{D_r}\right)^2, \quad 0\le k_r\le\frac{D_r}{\lambda\, f_l}\left(1-\frac{D_{r\_obs}}{D_r}\right) & \\ -2\left(\frac{D_{r\_obs}}{D_r}\right)^2+\frac{2\,D_{r\_obs}}{\pi\, D_r}\sin(\Theta)+\frac{1+\left(\frac{D_{obs}}{D_o}\right)^2}{\pi}\Theta & \\ \quad -2\,\frac{1-\left(\frac{D_{r\_obs}}{D_r}\right)^2}{\pi}\tan^{-1}\left[\left(\frac{1+\frac{D_{r\_obs}}{D_r}}{1-\frac{D_{r\_obs}}{D_r}}\right)\tan\left(\frac{\Theta}{2}\right)\right], & \frac{D_r}{\lambda\, f_l}\left(1-\frac{D_{r\_obs}}{D_r}\right)<k_r\le\frac{D_r}{\lambda\, f_l}\left(1+\frac{D_{r\_obs}}{D_r}\right)\\ 0, \quad k_r>\frac{D_r}{\lambda\, f_l}\left(1+\frac{D_{r\_obs}}{D_r}\right) & \end{cases}$$

$$\Theta=\cos^{-1}\left[\frac{1+\left(\frac{D_{r\_obs}}{D_r}\right)^2-\left(\frac{\lambda\, f_l\, k_r}{D_r}\right)^2}{2\,\frac{D_{r\_obs}}{D_r}}\right].$$

Optical Aberrations: A detailed aberration analysis[14] of deviations from ideal paraxial behavior of an optical system requires a designed optical system to analyze. In view of this paper's focus on optimal receiver system development rather than optical design, an OTF function that will establish a total aberration budget is called adequate. A Gaussian distribution function, where the OTF is attenuated by $e^{-1}$ at $k_r = \sigma_{ab}$ [cycles/m], is convenient and does reasonably well at approximating simple aberrations:

$$OTF_{ab}(k_r,\lambda)=e^{-\left[\frac{k_r}{|\Delta_{ab}|\frac{D_r}{\lambda\, f_l}}\right]^2}, \tag{13}$$

where,

$$\sigma_{ab} = \Delta_{ab} \frac{D_r}{\lambda f_l} \text{ [cycles/m]},$$

$\Delta_{ab}$ = scale factor.

Note that at $\Delta_{ab} = 1$, the aberrations OTF is reduced by 1/e at the annular aperture cutoff $k_o = D_o/\lambda_o f_l$ [cycles/m], a convenient reference point when establishing a budget (OTF degradation is minimal at $\Delta_{ab} = 1$, while at $\Delta_{ab} = ½$ the OTF degradation is quite noticeable).

Optical Defocus:[15] The defocus OTF approximates the effects of optical defocus depth and is useful in establishing focal depth tolerances:

$$OTF_{df}(k_r,\lambda) = \text{besinc}\left(\frac{1}{F\#^2} \Delta_{fs} \lambda \frac{k_r f_l}{D_r} \cdot \left(1 - \frac{k_r \lambda f_l}{D_r}\right)\right), \tag{14}$$

with the focal depth given as $\Delta_{fs} \cdot \lambda$ (the normalized focal shift is $\Delta_{fs} \cdot F\#^{-2}$ ), and besinc(x) = 2 $J_1(\pi x)/\pi x$.

Random Vibration:[16] For an rms amplitude vibrational displacement of $\sigma_v$ [m] (referenced to the image plane),

$$OTF_{rv}(k_r) = e^{-2\pi^2 \sigma_v^2 k_r^2}. \tag{15}$$

This OTF is used to establish system rms vibration and pointing stability tolerances. Note that this OTF does *not* properly account for systematic motion and various harmonic resonances which tends to vary from system to system. The rms pointing stability is given by $\tan^{-1}(\sigma_v / f_l)$ [radians].

Spatial Aperture:[17] The two-dimensional trapezoidal spatial quantization of a square pixel in the image plane is

$$OTF_{sa}(k_x,k_y) = \text{sinc}(k_x\, \Delta x)\, \text{sinc}(k_x\, (\Delta x - \delta x))\, \text{sinc}(k_y\, \Delta y)\, \text{sinc}(k_y\, (\Delta y - \delta y)), \tag{16}$$

where:

sinc(x)=sin(πx)/πx,
$\Delta x, \Delta y$ = pixel pitch [m],
$\delta x = \Delta x\, FF_x, \delta y = \Delta y\, FF_y$ = pixel dimension [m],
$FF_x, FF_y$ = fill factor.

Temporal Aperture:[18] (i) Degradation due to relative motion between the target and image plane, and (ii) Time-Delay and Integrate (TDI) synchronism error between target motion and TDI image plane electronic scan rate and discrete charge motion effects which applies only to Charge Coupled Devices (CCD) is determined through

$$OTF_{ta}(k_x,k_y) = \text{sinc}\left[\frac{\tau_o f_l}{n_{cp} R}\left(k_x(V_x + \Delta V_x) + k_y(V_y + \Delta V_y)\right)\right] \frac{\text{sinc}\left[\frac{\tau_o f_l}{R}\left(k_x\, \Delta V_x + k_y\, \Delta V_y\right) n_{tdi}\right]}{\text{sinc}\left[\frac{\tau_o f_l}{R}\left(k_x\, \Delta V_x + k_y\, \Delta V_y\right) \frac{1}{n_{cp}}\right]}, \tag{17}$$

where:

sinc(x)=sin(πx)/πx,
$R$ = aperture to target range [m],
$f_l$ = effective focal length [m],

$V_x$, $V_y$ = relative differential velocity between image-plane and target [m/s],
$\tau_o$ = integration period [s].

The following apply only to scanning TDI focal planes:

$n_{tdi}$ = number of TDI stages,
$n_{cp}$ = number of clock phases per sample (CCD only),
$\Delta V_x$, $\Delta V_y$ = relative velocity error [m/s] between target and TDI image plane electronic scan rate and discrete charge motion effects (CCD only), else default to $n_{tdi} = n_{cp} = 1$, and $\Delta V_x = \Delta V_y = 0$.

Additional technology and application specific OTF components not discussed include detector carrier diffusion in CCD focal plane arrays,[19, 20, 21] detector, amplifier and readout bandwidth limitations and OTF deficiencies that can be can be partially compensated for with signal processing. [22, 23] The effects of these OTF components *should* be considered as the system design progresses towards a specific hardware technology.

Finally, evaluation of the degradation factor due to resolution is given by the ratio

$$\zeta_{res}(R) = \frac{\iint\limits_{A_d} PSF_o * I_{xr}\left(R, M_o(R)\cdot x, M_o(R)\cdot y\right) \; dx\,dy}{\iint\limits_{A_d} I_{xr}\left(R, M_o(R)\cdot x, M_o(R)\cdot y\right) \; dx\,dy}, \qquad \textbf{(18)}$$

where $A_d$ is the image plane active detection area, $M_o(R) = \left|\frac{R - Z_{r\_obs}}{f_l}\right|$ the optical magnification, $PSF_o$ the optical PSF *up to* the surface of the image plane (see **Equation 29 in Section 2.1.E**), and $I_{xr}$ the imaged transmitter/receiver overlap intensity given by **Equation 5**.

### 2.1.D. Combined effect of GFF and resolution

**Figure 5** illustrates how the combined effects of resolution and GFF degrade and modulate detected intensity. Ideally, the received beam profile is undistorted and centered over the active detection area with 100% of the beam intensity accounted for when integrated over the active detection area. However, geometric factors including transmitter to receiver overlap/alignment, and near-field receiver obstruction will distort and displace the intensity distribution, effectively reducing detection efficiency by attenuating and clipping the beam when integrated over the active detection area. Compounding the effect, insufficient resolution broadens the intensity distribution further reducing detection efficiency. In general, a performance trade can be expected between detection noise and GFF for single element detectors. A large detector may achieve a 100% GFF efficiency but generate excessive detection noise, while a small detector with lower noise may have a low GFF efficiency and potentially introduce correlated noise by detected signal modulation through systematic intensity clipping at the detector. Properly implemented, a detector array may provide for both high GFF efficiencies and low detection noise as well as improved target acquisition. Detection noise will be introduced in **Section 2.2.** and the GFF/detection-noise trade further elaborated in **Section 3**.

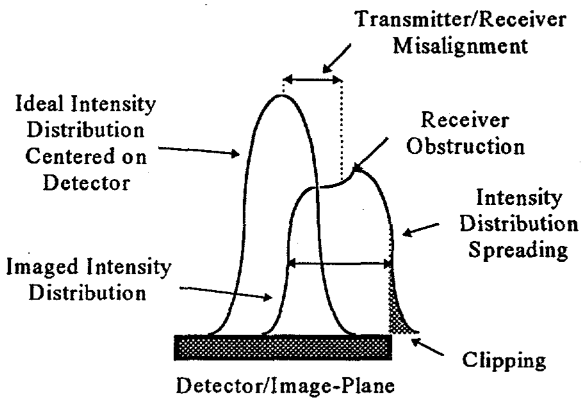

**Figure 5.** Combined Effects of GFF and Optical Resolution on Detected Intensity.

### 2.1.E. Target sampled distance, effective resolution, and sampling criteria

For efficient performance analysis of imaging arrays, the raw OTF/PSF information generated should be processed and reduced to a set of parameters that efficiently summarizes system performance. While the ability to examine each and every OTF/PSF component may be important, a reduced set of representative parameters will aid in defining, designing and characterizing the receiver. The parameters, target sampled distance, effective resolution, and sample rate are defined in this section.

Target Sampled Distance (TSD): The TSD is the geometric-optics projection of the pixel in the image plane onto the target. For pixel pitch $\Delta x$, $\Delta y$, range-to-target $R$, and effective system focal length $f_l$, the projected TSD in Cartesian coordinates is

$$TSD_x = \Delta x \frac{R}{f_l}, \qquad TSD_y = \Delta y \frac{R}{f_l}. \tag{19}$$

Related to the TSD is the number of pixels or samples, per dimension, required to cover the target area given by the product of $L_x L_y$

$$N_{pix\_x} = \frac{L_x}{TSD_x}, \qquad N_{pix\_y} = \frac{L_y}{TSD_y}. \tag{20}$$

Hence, for a fixed target area coverage rate, **Equation 20** indicates a trade between resolution and the number of pixels/samples required. Note that the number of pixels/samples determines the receiver's data collection processing rate and storage requirements, which can become an important system consideration.

Effective Resolution: Considering the composition of $OTF_{sys}$ given in **Equation 8**, the TSD is generally not an accurate representation of the receiver's effective resolution due to probable contributions from other OTF components. A preferred measure of resolution is one that incorporates the full system OTF/PSF. Shade's equivalent passband $^3$ approach estimates the PSF spread by evaluating the OTF's equivalent bandwidth and inverting,

$$\Delta_{psf\_x} = \frac{1}{2\int_0^\infty \left|OTF_{sys}(k,0,\lambda_o)\right|^2 dk}, \qquad \Delta_{psf\_y} = \frac{1}{2\int_0^\infty \left|OTF_{sys}(0,k,\lambda_o)\right|^2 dk}. \tag{21}$$

This concept is very similar to the noise equivalent bandwidth approach used when relating pulsewidth and noise bandwidth (see also Fourier uncertainty principle that can be found in most communication text books). While this technique is appropriate for most well-behaved OTF's, a second technique that operates directly on the PSF should be considered as a cross-check. The integrated intensity effective resolution integrates over the intensity of the PSF

$$\Delta_{psf\_x} = 2\,\xi, \quad given \quad \frac{\int_0^\xi \left|PSF_{sys}(x,0)\right| dx}{\int_0^\infty \left|PSF_{sys}(x,0)\right| dx} = 1-\Delta I, \quad \Delta_{psf\_y} = 2\,\xi, \quad given \quad \frac{\int_0^\xi \left|PSF_{sys}(0,y)\right| dy}{\int_0^\infty \left|PSF_{sys}(0,y)\right| dy} = 1-\Delta I. \tag{22}$$

where $\Delta I$ is the fractional integrated intensity error (typically ~ 0.05). For well behaved OTF/PSFs, both the Shade's equivalent pass band and the integrated intensity evaluate PSF spreads will differ by only a few percent. Finally, the target-projected effective resolution, given a point source is

$$RES_x = \Delta_{psf\_x} \frac{R}{f_l}, \qquad RES_y = \Delta_{psf\_y} \frac{R}{f_l}. \tag{23}$$

Note that the effective resolution (RES) approaches the pixel TSD when $PSF_{sa}$ dominates the system point spread function.

The diameter of the first zero of the Airy pattern of a circular aperture's PSF is a familiar measure and will be applied in the following sampling criteria. Applying the inverse Fourier transform to the circular aperture portion of **Equation 11-12** ($D_{r\_obs}=0$) and solving for the first zero,

$$\pi\left(\frac{D_r}{2}\right)^2 \text{besinc}\left(\frac{k\,D_r\,r}{2\,\pi\,f_l}\right)^2 \rightarrow 0 \quad @ \quad r \approx 1.22\frac{\lambda\,f_l}{D_r}, \quad k=\frac{2\,\pi}{\lambda},$$

results in an Airy disk diameter of $\delta_{ap} = 2.44\dfrac{\lambda\,f_l}{D_r}$ (the diffraction limit). **(24)**

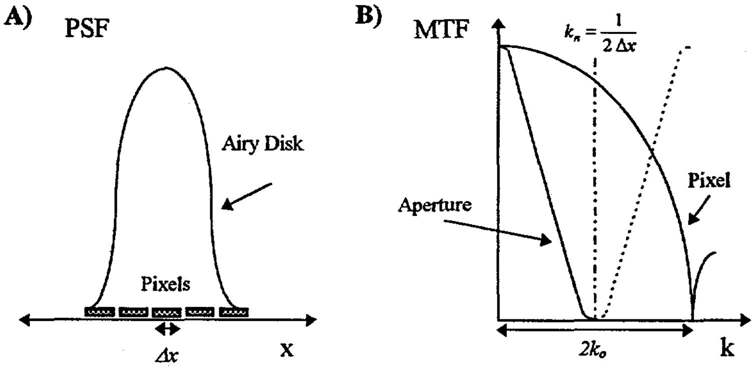

**Figure 6.** Spatial and Frequency Domain Illustration of a Nyquist Sampled Circular Aperture: A) 4.88 pixels per dimension under the Airy disk, and **B)** aperture cutoff, $k_o$, equal to the pixel Nyquist frequency, $k_n$, which is half the Nyquist rate of $2k_o$. Sampling at a rate of less then $2k_o$ can overlap and alias the adjacent spectra (dotted curve) about the Nyquist frequency $k_n$.

Sampling Criteria: For the unique reconstruction of a sampled image, the Whittaker-Shannon sampling theorem[9, 24, 25, 26] requires a uniform sample spacing of no less than

$$\Delta x = \frac{1}{2\,k_n}, \tag{25}$$

where $k_n$ is the highest resolvable spatial frequency contained the image. The sample rate of $2k_n$ [cycles/m] is known as the Nyquist rate and

$$k_n = \frac{1}{2\,\Delta x} \tag{26}$$

the Nyquist frequency. Any spatial frequencies below the Nyquist frequency will be unambiguously reconstructed while spatial frequencies above the Nyquist frequency may be *aliased*[27, 28] to a lower frequency. Applying the sampling theorem to the circular aperture portion of **Equation 11-12** ($D_{r\_obs} = 0$), the high-frequency cutoff, $k_o$, is $k_o = \dfrac{D_r}{\lambda\,f_l}$. From **Equation 25**, for the case of square pixels, Nyquist sampling requires

$$\Delta x = \Delta y = \frac{\lambda\,f_l}{2\,D_r}, \tag{27}$$

where $\Delta x$ and $\Delta y$ are the single pixel dimensions defined in **Equation 16** (100% fill factor assumed). The number of pixels under the Airy disk diameter from **Equation 24** is then

$$\frac{\delta_{ap}}{\Delta x} = \frac{\delta_{ap}}{\Delta y} = \frac{2.44\,\dfrac{\lambda\,f_l}{D_r}}{\dfrac{\lambda\,f_l}{2\,D_r}} = 4.88 \quad \text{pixels.} \tag{28}$$

**Figure 6** illustrates the spatial and frequency domain representation of a Nyquist sampled circular aperture. The sampling theorem can next be applied to the general optical OTF

$$OTF_o(k_x,k_y,\lambda_o) = OTF_{rv}(k_x,k_y,\lambda_o)\cdot OTF_{df}(k_x,k_y,\lambda_o)\cdot OTF_{ab}(k_x,k_y,\lambda_o)\cdot OTF_{ap}(k_x,k_y,\lambda_o)\cdot OTF_{atm}(k_x,k_y,\lambda_o), \tag{29}$$

by developing an equivalent PSF spread sampling criteria. The equivalent PSF spread of the circular aperture (**Equations 11-12,** $D_{r\_obs} = 0$) using Shade's equivalent passband evaluates to

$$\Delta_{cir} = \frac{1}{2\int_0^\infty \left|OTF_{ap\_cir}\right|^2 dk} = \left[2\int_0^\infty \left|\frac{2}{\pi}\left(\cos^{-1}(r) - r\sqrt{1-r^2}\right)\right|^2 dr\right]^{-1} \frac{\lambda f_l}{D_r} = 1.835\frac{\lambda f_l}{D_r}, \tag{30}$$

where 1.835 is the circular aperture form factor. The sampling theorem requires,

$$\frac{\Delta_{cir}}{\Delta x} = \frac{\Delta_{cir}}{\Delta y} = \frac{1.835\frac{\lambda f_l}{D_r}}{\frac{\lambda f_l}{2\,D_r}} = 3.67, \tag{31}$$

and, an equivalent sampling rate can be estimated with

$$S_{r\_x} = \frac{\Delta_o}{3.67\,\Delta x}, \qquad S_{r\_y} = \frac{\Delta_o}{3.67\,\Delta y}, \tag{32}$$

where from **Equation 21**

$$\Delta_o = \frac{1}{2\int_0^\infty \left|OTF_o(k,0,\lambda_o)\right|^2 dk}. \tag{33}$$

A sample rate ($S_r$) of 1.0 implies Nyquist rate sampling with 4.88 pixels per Airy disk diameter per dimension as illustrated in **Figure 7**. Approximately twenty pixels per Airy disk is a costly proposition and is probably unnecessary for most applications. A sample rate of 0.2 to 0.5 (one to three pixels per Airy disk diameter) should be used as a synthesis target for imaging systems with nominal resolution and aliasing requirements. Sample rates of 0.5 to 1.0 should be considered for high resolution systems or when imaging scenes contain high spatial uniformity.

## 2.2. Signal Detection in the Presence of Noise

Two dominant hard-target return DIAL noise classes are considered in this paper: speckle and detection noise. Expanding **Equation 1**, the effective receiver SNR for a single return pulse will be defined as

$$SNR = \sqrt{\frac{1}{\frac{1}{SNR^2_{speckle}} + \frac{1}{SNR^2_{detection}}}}, \tag{34}$$

where it has been assumed that the noises are uncorrelated. Note that **Equation 34** implies that receiver SNR may be dominated by either speckle or detection noise (speckle is *not* present in incoherent passive systems). The remainder of **Section 2** will be devoted to explicitly defining and modeling the noise components of **Equation 34**.

### 2.2.A. Speckle

The speckle pattern viewed in the optical image plane of a DIAL receiver is a consequence of random phase aberrations introduced on an otherwise coherent optical field at the object plane.[29, 30, 31, 32, 33] Viewed in the image plane, the speckle density is proportional to the spatial or spectral composition of the object-plane field, which for a rough, hard-target DIAL is determined by the beam-shape and distribution, range to target, and the receiver's resolution (see PSF or MTF of **2.2.B.**). The SNR of the detected intensity of a single-shot DIAL measurement due to rough target speckle is proportional to the square root of the total number of statistically independent speckle nodes in the image plane - a manifestation of negative exponential statistics of rough target speckle[34]. Hence, for a given receiver with clear aperture diameter $D_r$ and an effective diameter at target $D_{xt}(R)$ (Gaussian beam, **Equation 4** at range $R$), the speckle SNR is evaluated with[35]

$$SNR_{speckle} = \left[ \frac{16}{\pi} \int_0^1 \left( \cos^{-1}(r) - r\sqrt{1-r^2} \right) e^{-\pi\left(\frac{D_{xt}(R)\,D_r}{\lambda_o\,R} r\right)} r\,dr \right]^{-\frac{1}{2}}, \tag{35}$$

where $\lambda_o$ is the laser wavelength. Providing some insight into the key relations governing speckle SNR, **Equation 35** can be approximated by

$$SNR_{speckle} \approx \sqrt{1 + \left( \frac{D_{xt}(R)\,D_r}{\lambda_o\,R} \right)^2}\ . \tag{36}$$

**Equation 36** shows that the speckle SNR increases for larger beam and receiver diameters and *appears* to decrease to unity for very long ranges. Realistically, a propagating laser beam will always exhibit some degree angular divergence (again, $\theta_x$ of **Equation 4**) increasing $D_{xt}$ as a function of range such that the $R$ in **Equation 36** is partially compensated resulting in a relatively constant $SNR_{speckle}$ vs. range. As was discussed in **Section 2.1.D** (GFF/detection-noise trade), a speckle/detection noise trade will exist between speckle SNR (larger FOV→ larger detector), the detection SNR (smaller detector → smaller FOV) for single element detectors, and the target under resolution.

### 2.2.B. Signal irradiance at detector: extended hard-target return

The received signal power at the detector surface, given an extended, flat, diffuse (rough) target is approximated by the modified RADAR range equation[36]

$$P_s(R) = P_x\ \eta_x\ \frac{T_a(R)^2\ \xi_{xr}(R)\,\xi_{res}(R)\,D_r\ \eta_r}{2\,R^2}\ \rho\cos(\theta), \tag{37}$$

where $P_x$ and $\eta_x$ are the effective transmitted laser pulse power and optical transmission efficiency, respectively, the one way atmospheric transmission over range $R$, $T_a(R) = e^{-\int_R \alpha(r)\,dr}$, $\xi_{xr}$ and $\xi_{res}$ the optical efficiencies defined by **Equations 2** and **18**, $D_r$ the receiver clear aperture diameter, and $\eta_r$ the receiver optical transmission efficiency ($\eta_r = T_{optics}$ x $T_{filter}$). The view angle, measured from zenith, and mean reflectivity modeling the extended surface, $\rho\cos(\theta)$, are $\theta$ [rad] and $\rho$ [], respectively. The signal irradiance, at the detector surface, is related to the received signal power $P_s$ through

$$\Phi_s = \frac{\lambda_o}{h \cdot c} \cdot \frac{1}{A_d} \cdot P_s \quad \text{[ph/m}^2\text{-s]}, \tag{38}$$

where $\lambda_o$ is the laser wavelength, and $A_d$ is the active detection area. $\Phi_s$ for passive imaging can be found in *Methodology for Rapid Infrared Multi-Spectral, Electro-Optical Imaging System Performance and Synthesis* [37].

### 2.2.C. Detection Noise

Detection noise, as illustrated in **Figure 7**, can be broken into three primary components: (1) photon noise, (2) detector, amplifier, readout, and processing noise, and (3) systematic noise. The mean signal-to-noise ratio *referenced at the detector* is

$$SNR_{detection} = \frac{\Phi_s}{NEI_{tot}} \quad \text{[ph-m}^{-2}\text{-s}^{-1}\text{/ ph-m}^{-2}\text{-s}^{-1}\text{]}, \tag{39}$$

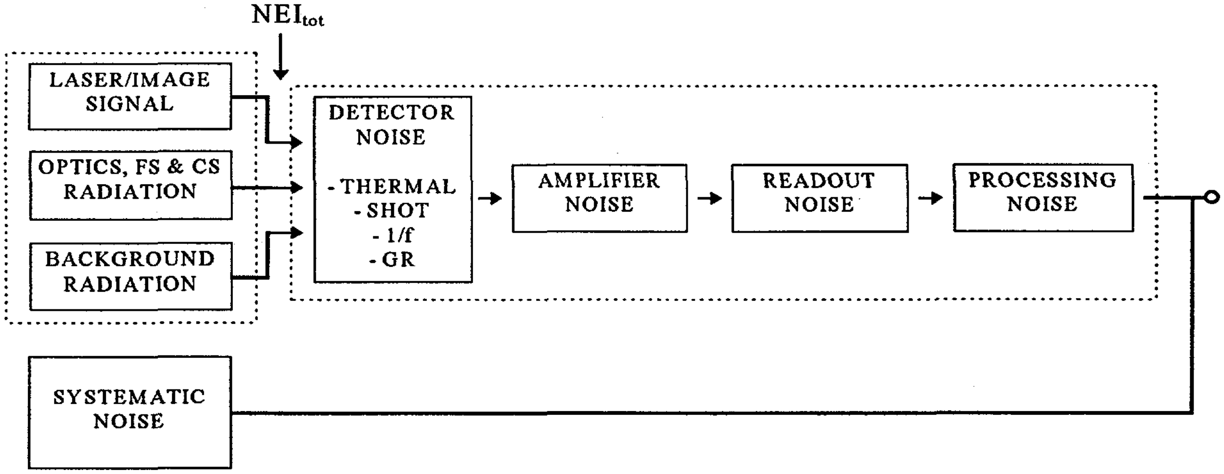

**Figure 7.** Detection Noise. Note: FS ≡ field-stop, CS ≡ cold-shield, 1/f ≡ one-over frequency noise, and GR ≡ generation recombination.

where:

$$\Phi_s = \frac{\lambda_o}{h \cdot c} \cdot \frac{1}{A_d} \cdot P_s$$ signal irradiance (**Equation 38**),

$$NEI_{tot} = \sqrt{NEI_{ph}^2 + NEI_{dar}^2 + NEI_{sys}^2}$$ total noise equivalent irradiance,

$$NEI_{ph}^2 = NEI_s^2 + NEI_{op}^2 + NEI_{fs}^2 + NEI_{cs}^2 + NEI_{bg}^2$$ photon noise: signal + optics + field-stop + cold-shield + background,

$$NEI_{dar}^2 = NEI_{det}^2 + NEI_{amp}^2 + NEI_{ro}^2 + NEI_{dig}^2$$ electronic noise: detector + amplifier + readout + digitization,

$$NEI_{sys}^2 = NEI_{xt}^2 + \ldots$$ systematic: cross-talk + .... etc.

All of the above noise equivalent irradiances are *referenced at the detector*. The selection of the surface of the detector as the SNR reference point needs some elaboration. When evaluating the detection SNR, the *Signal* and detection noise can be referenced at any point in the system – at the aperture, between the optical train and filter, at the detector, at the amplifier etc. This paper references the surface of the detector because it is an electro-optical system's natural *optical ↔ electronic* interface. Everything to the "left" of the interface lies in the optical domain, while to the "right" in the electronic domain (the interface is illustrated in **Figure** 7, $NEI_{tot}$, which falls between the dashed boxes).

### 2.2.C.1. Photon noise

The photon noise sources are diagrammed in **Figure 8**, where the optics, field-stop, and cold-shield are modeled as gray body thermal sources, while the background radiance can cover, in general, a broader spectrum. Note that a good design requires the proper matching of system and cold-shield solid angle, i.e. $\Omega_{cs} \le \Omega_{sys}$, with $\Omega_{sys} = \frac{\pi}{4\left(\frac{f_l}{D_o}\right)^2}$ [sr].

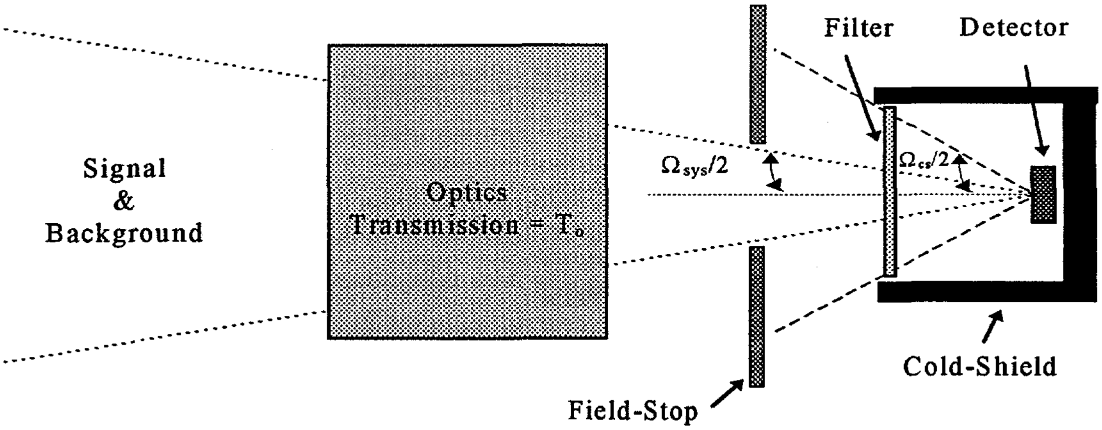

**Figure 8.** Photon Noise Sources.

Expressions evaluating the noise equivalent irradiance for signal, background, optical train, field-stop, and cold shield follow.

Signal:

$$NEI_s = \sqrt{\kappa_d \frac{\Delta f}{A_d\ \eta_d(\lambda_o)} \Phi_s} \qquad \text{[ph/m}^2\text{-s]} \tag{40}$$

Where $\Delta f$ is the electronic noise equivalent bandwidth in Hertz given by

$$\Delta f = \frac{\int_0^\infty |G(f)|^2\, df}{|G_{max}|^2} \qquad \text{[Hz]}, \tag{41}$$

with G(f) the detector/amplifier/readout electronic transfer function, $\eta_d$ the detection quantum efficiency at $\lambda_o$, and $\kappa_d$ the noise process scale factor ($\kappa_d = 2$ for a photovoltaic and $\kappa_d = 4$ for photoconductor).

Background:

$$NEI_{bg} = \sqrt{\frac{\kappa_d\ \Delta f\ \Omega_o}{A_d\ h\ c} \int_0^\infty \frac{1}{\eta_d(\lambda)} L_{bg}(\lambda)\, \chi(\lambda)\, \lambda\, d\lambda} \qquad \text{[ph/m}^2\text{-s]} \tag{42}$$

Where

$$\chi(\lambda) = \chi_o + \chi_s\, e^{-\left|\frac{\lambda-\lambda_o}{\left(\frac{\lambda_2-\lambda_1}{2}\right)}\right|^{\chi_e}} \tag{43}$$

is the spectral transmission function applicable to the development and modeling of spectrally tunable or multi-band DIAL receivers with the following properties:

i) The average passband transmission, $\chi_s = T_o\, T_f$, is the product of optical train and filter transmissions.
ii) The average stopband transmission, $\chi_o$.
iii) Adjustable filter strength, $\chi_e$, is the function's exponential coefficient that can range from a simple Gaussian filter for $\chi_e = 2$, to a near ideal filter for $\chi_e >> 10$.

iv) A well defined band center, $\lambda_o = \lambda_1 + \frac{\lambda_2 - \lambda_1}{2}$ , and passband/stopband edges, $\lambda_1$ and $\lambda_2$ (1/e band-edges), that do not shift as a function of filter strength.

Finally, $\Omega_o = \left(1 - \left(\frac{D_{obs}}{D_o}\right)^2\right) \cdot \frac{\pi}{4 \cdot \left(\frac{f_l}{D_o}\right)^2}$ [sr], is the effective solid angle subtended by the optical aperture, $D_o$ the diameter of clear aperture, $D_{obs}$ the diameter of the clear aperture obstruction, $f_l$ the effective system focal length , $L_{bg}(\lambda)\, d\lambda$ [W/m$^2$-sr] the background radiance, $h = 6.626 \cdot 10^{-34}$ [J-s] is Plank's constant, and $c = 2.998 \cdot 10^8$ [m/s] the speed of light.

In practice, the detector has a finite response and the quantum efficiency, $\eta_d(\lambda)$, can be replaced by its average value, $\eta_d$, and the limits of the integral can be substituted for the effective quantum efficiency bandwidth, $\lambda_{\eta 1} \rightarrow \lambda_{\eta 2}$. The spectral efficiency reduces to

$$NEI_{bg} = \sqrt{\frac{\kappa_d\ \Delta f\ \Omega_o}{A_d\ \eta_d\ h\ c} \int_{\lambda_{\eta 1}}^{\lambda_{\eta 2}} L_{bg}(\lambda)\ \chi(\lambda)\ \lambda\ d\lambda} \qquad \text{[ph/m}^2\text{-s]} \qquad \textbf{(44)}$$

which simplifies design and computer analysis by removing the $0 \rightarrow \infty$ limit.

Optical Train:

$$NEI_{op} = \sqrt{\frac{\kappa_d\ \Delta f}{A_d\ \eta_d\ h\ c} \frac{\Omega_{sys}}{\pi} \int_{\lambda_{\eta 1}}^{\lambda_{\eta 2}} \sum_i M_{op}\left(T_{op_i}, \varepsilon_{op_i}, \lambda\right) \frac{\chi(\lambda)}{T_{o_i}}\ \lambda\ d\lambda} \qquad \text{[ph/m}^2\text{-s]} \qquad \textbf{(45)}$$

Here each optical element or optical subsystem, i=1,2,3,..n, contributes to the near-field thermal exitance $M_{op}$. Note how the remaining optical transmission from the i$^{th}$ component to the detector surface is maintained by dividing the system transmission $\chi(\lambda)$ by the i$^{th}$ component of $T_o$. In many cases, *apriori* knowledge of the number, position, temperature, and material properties of the optical elements is unavailable during the preliminary design phase. However, an NEI$_{op}$ budget can be allocated by approximating the thermal exitance with a single source,

$$NEI_{op} = \sqrt{\frac{\kappa_d\ \Delta f}{A_d\ \eta_d\ h\ c} \frac{\Omega_{sys}}{\pi} \int_{\lambda_{\eta 1}}^{\lambda_{\eta 2}} M_{op}\left(T_{op}, \varepsilon_{op}, \lambda\right) \frac{\chi(\lambda)}{T_o}\ \lambda\ d\lambda} \qquad \text{[ph/m}^2\text{-s].} \qquad \textbf{(46)}$$

Typically, an $\varepsilon_{op} \sim 0.05 - 0.1$ @ $T_{op} = 300$ K will suffice for uncooled optics, where $\varepsilon_{op}$ = effective emissivity, and $T_{op}$ [°K] is the effective temperature.

Field Stop:

$$NEI_{fs} = \begin{cases} 0 \quad if \quad \Omega_{cs} \le \Omega_{sys}, \quad else \\ \sqrt{\frac{\kappa_d\ \Delta f}{A_d\ \eta_d\ h\ c} \frac{\left(\Omega_{cs} - \Omega_{sys}\right)}{\pi} \int_{\lambda_{\eta 1}}^{\lambda_{\eta 2}} M_{fs}\left(T_{fs}, \varepsilon_{fs}, \lambda\right) \frac{\chi(\lambda)}{T_o}\ \lambda\ d\lambda} \end{cases} \qquad \text{[ph/m}^2\text{-s]} \qquad \textbf{(47)}$$

Cold-Shield:

$$NEI_{cs} = \sqrt{\frac{\kappa_d\ \Delta f}{A_d\ \eta_d\ h\ c} \frac{\left(\pi - \Omega_{cs}\right)}{\pi} \int_{\lambda_{\eta 1}}^{\lambda_{\eta 2}} M_{cs}\left(T_{cs}, \varepsilon_{cs}, \lambda\right) \frac{\chi(\lambda)}{T_o}\ \lambda\ d\lambda} \qquad \text{[ph/m}^2\text{-s]} \qquad \textbf{(48)}$$

The exitance functions, $M_{op}$, $M_{fs}$, and $M_{cs}$ are of the form

$$M(T,\varepsilon,\lambda)\,d\lambda = \frac{2\,\pi\,h\,c^2}{\lambda^5}\,\varepsilon\,e^{\frac{h\,c}{\lambda\,k_b\,T}}\,d\lambda \quad [\mathrm{W/m^2}], \tag{49}$$

where $k_b = 1.381 \cdot 10^{-23}$ [J/K] Boltzmann's constant, $\varepsilon$ = emissivity, and $T$ [°K] = temperature. Background radiance, $L_{bg}(\lambda)$ $d\lambda$ [w/m$^2$-sr], from a given scene that includes complex transmission, backscatter, and emission effects can be generated with computer simulation tools such as LOWTRAN,[38] MODTRAN or HITRAN/FASCODE.

### 2.2.C.2. Detector, amplifier and readout response and noise

The following models deal with the response and noise of the classic photovoltaic detector and transimpedance amplifier topology and are an expanded version of an unpublished collection of analysis techniques and models by T. Lomheim and J. Johnson[39]. Inasmuch as the analysis techniques used to derive the models in this section are rather standard and widely used, only the results are listed with the interested reader referred to selected sources. [40, 41, 42, 43] Referring to the generic photovoltaic detector and transimpedance amplifier circuit of **Figure 9**, the remainder of this section summarizes the detector, amplifier and readout modeling parameters and lists the respective electro-optic response and noise models.

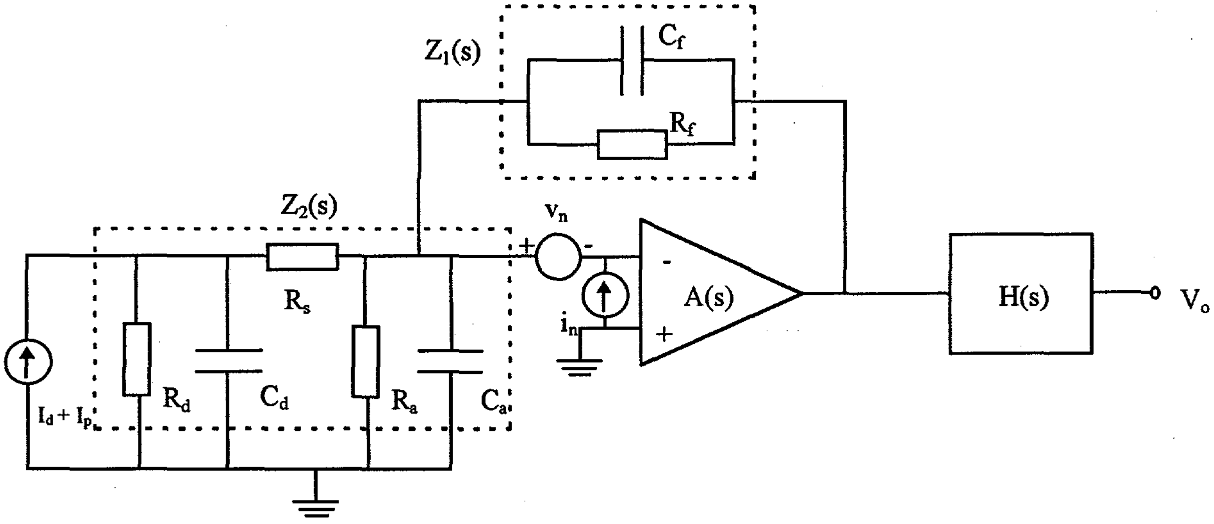

**Figure 9.** Generic Photovoltaic Detector and Transimpedance Amplifier Circuit Used in Electro-Optic Response and Noise Analysis.

<u>**Detector and Amplifier Parameters**</u>

Detector:

$A_d$ [m$^2$]: active detection area (single element or FPA pixel),
$R_d$ [Ω]: dynamic impedance (at bias voltage),
$R_s$ [Ω]: series resistance,
$C_d$ [F]: junction capacitance (at bias voltage),
$I_d$ [A]: dark current (at bias voltage),
$I_p$ [A]: photocurrent,
$k_{1/f\_d}$ []: 1/f coefficient,
$T_d$ [K]: detector temperature.

Amplifier:

$GB$ [Hz]: gain - bandwidth product,
$f_a$ [Hz]: open loop -3db frequency (1st order approximation),
$A(s)=\dfrac{2\pi GB}{s+2\pi f_a}$ [V/V]: frequency dependent voltage gain (1st order approximation) and $s = 2\pi i f$ (Laplace variable),
$R_a$ [Ω]: equivalent real resistance seen at amplifier input due to external bias networks etc. (not including $R_d$ & $R_f$),
$C_a$ [F]: total equivalent amplifier input capacitance not including $C_d$ and $C_f$,
$R_f$ [Ω]: feedback resistance ($R_f \rightarrow \infty$ for capacitive transimpedance amplifier (CTIA) configurations),
$C_f$ [F]: feedback capacitance (integrating capacitor in CTIA configurations),
$v_{n\_a}$ [V/√Hz]: input noise voltage,
$f_{v\_1/f\_a}$ [Hz]: input noise voltage 1/f corner,
$i_{n\_a}$ [A/√Hz]: input noise current,
$f_{i\_1/f\_a}$ [Hz]: input noise current 1/f corner,
$T_a$ [K]: amplifier temperature.

Frequency Dependent Transfer Function H(s):

The modeling of signal filtering and conditioning, readout circuitry, and processing is approximated by *H(s)*. For example, an ideal sampling integrator (integration/sample window = $\tau_o$) would be modeled as (note $s \rightarrow 2\pi i f$)

$$H(f)=e^{-i\pi f \tau_o}\,\frac{\sin(\pi f \tau_o)}{\pi f \tau_o}. \qquad \textbf{(50)}$$

## Response and Noise Models

Detector Response:

The photocurrent of the photovoltaic detector induced by $P_p$ watts of incident optical power at wavelength $\lambda_o$ is

$$I_p = q\,\frac{\lambda_o}{h\,c}\,\eta_d\,P_p \quad \text{[A].} \qquad \textbf{(51)}$$

Transimpedance Gain:

Given an optically induced signal current of $I_p = 1$ Ampere, the frequency dependent output voltage response, $V_o$, to source, $I_p$, is defined by the transimpedance function

$$Z_T(s)=\frac{R_d}{R_d+R_s+C_d\,R_d\,R_s\,s}\;\frac{Z_1(s)}{1+\dfrac{1}{A(s)}\left(1+\dfrac{Z_1(s)}{Z_2(s)}\right)}\,H(s) \quad \text{[V/A],} \qquad \textbf{(52)}$$

where

$$Z_1(s)=\frac{R_f}{1+R_f\,C_f\,s}, \quad \text{and} \quad Z_2(s)=\left[\left(R_s+\frac{R_d}{1+R_d\,C_d\,s}\right)^{-1}+\left(\frac{R_a}{1+R_a\,C_a\,s}\right)^{-1}\right]^{-1}.$$

Responsivity:

Combining **Equation 51** and **52**, the response of the circuit to one watt of incident optical power at wavelength, $\lambda_o$, and electrical frequency, $f_o$, provides the following relation defining the circuit's responsivity,

$$\Re(\lambda_o, f_o) = q \frac{\lambda_o}{h\,c} \eta_d \left|Z_T(2\pi i f_o)\right| \quad \text{[V/W]}. \tag{53}$$

Root-Mean-Square (RMS) output noise voltage [V]:

The RMS output referenced noise voltage is given by integrating over the output referenced noise voltage spectral density,

$$v_{rms} = \sqrt{\int_0^\infty v_{n\_o}^2(f)\, df} \quad \text{[V]}, \tag{54}$$

where the voltage spectral density is given by,

$$v_{n\_o}(f) = \sqrt{\left[ v_n^2(f) \left| \frac{1 + \frac{Z_1(2\pi i f)}{Z_2(2\pi i f)}}{1 + \frac{1}{A(2\pi i f)}\left(1 + \frac{Z_1(2\pi i f)}{Z_2(2\pi i f)}\right)} \right|^2 + i_n^2(f) \left| \frac{Z_1(2\pi i f)}{1 + \frac{1}{A(2\pi i f)}\left(1 + \frac{Z_1(2\pi i f)}{Z_2(2\pi i f)}\right)} \right|^2 \right] \left|H(2\pi i f)\right|^2} \quad \text{[V/}\sqrt{\text{Hz}}\text{]}, \tag{55}$$

with the input referenced voltage and current noise density

$$v_n(f) = \sqrt{\left(v_{n\_a}\left(1 + \frac{1}{f} f_{v\_1/f\_a}\right)\right)^2} \quad \text{[V/}\sqrt{\text{Hz}}\text{], and} \tag{56}$$

$$i_n(f) = \sqrt{\begin{gathered} \left(2\,q\,(I_d + I_p) + \frac{4\,k\,T_d}{R_d} + \frac{k_{1/f\_d}^2\, I_d^2}{f}\right) \left|\frac{R_d}{R_d + R_s + 2\pi i f\, R_d\, C_d\, R_s}\right|^2 + \frac{4\,k\,T_d\,R_s}{\left|R_s + \frac{R_d}{1 + 2\pi i f\, R_d\, C_d}\right|^2} \\ + \left(\frac{4\,k\,T_a}{\frac{R_f\,R_a}{R_f + R_a}} + \left(i_{n\_a}\left(1 + \frac{1}{f} f_{i\_1/f\_a}\right)\right)^2\right) \end{gathered}} \quad \text{[V/}\sqrt{\text{Hz}}\text{]}. \tag{57}$$

As an aid to understanding noise propagation, let $A(f) \to \infty$ and $R_s \to 0$ of **Equation 55** resulting in the following simplified output referenced voltage spectral density [V/Hz]

$$v_{n\_o}(f) = \sqrt{\left[ v_n^2(f)\Big|_{R_s \to o} \left| 1 + \frac{R_f}{\frac{R_d\,R_a}{R_d + R_a}} \frac{1 + 2\pi i f \frac{R_d\,R_a}{R_d + R_a}(C_d + C_a)}{1 + 2\pi i f\, R_f\, C_f} \right|^2 + i_n^2(f)\Big|_{R_s \to o} \left| \frac{R_f}{1 + 2\pi i f\, R_f\, C_f} \right|^2 \right] \left|H(2\pi i f)\right|^2}. \tag{58}$$

A typical output referenced noise spectral density generated by **Equation 58** is plotted in **Figure 10**. Three spectral regions can generally be identified: 1) low frequency 1/f noise, due to both detector and amplifier, 2) a mid-band white noise floor, and 3) the high frequency noise "boosting" of input referenced noise voltage, $v_n$, due primarily to detector and amplifier capacitance. Both the low frequency and high frequency "excess" noise (noise above the mid-band floor) are detrimental to receiver performance. Low-frequency 1/f noise introduces correlated statistics into DIAL multi-shot averaging (see **Section 2.2.E**), while high frequency noise very quickly limits the practical usable bandwidth (high frequency noise will dominate **Equation 54**). As will be discussed in **Section 3**, the noise sources and the response of H(s) modeled in **Equation 58** can be minimized and shaped, respectively, for an optimal DIAL detection SNR.

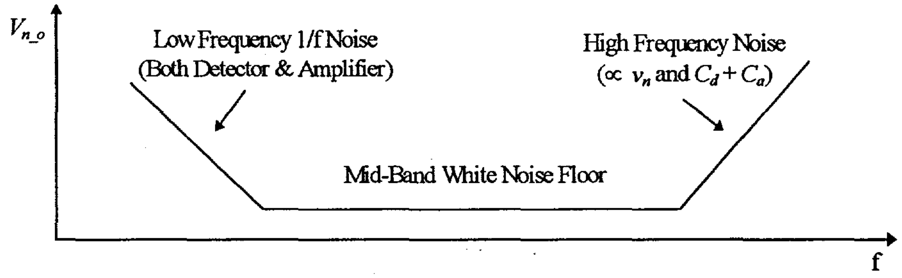

**Figure 10.** Typical Noise Spectrum Generated by **Equation 58** when H(s) =1.

RMS Noise Equivalent Power Referenced at Detector Surface (NEP):

$$NEP(\lambda_o) = \frac{h\,c\,A_d}{\lambda_o}\,NEI = \frac{h\,c}{\lambda_o\,\eta_d}\sqrt{\int_0^{f_{3db}} \frac{v_{n\_o}^2(f)}{\left|Z_T(2\pi i f)\right|^2}\,df} \approx \frac{h\,c}{\lambda_o\,\eta_d}\,\frac{v_{rms}}{\left\langle \left|Z_T\right| \right\rangle} \quad [\mathrm{W}]. \tag{59}$$

Noise Equivalent Bandwidth (NEB):

From **Equations 41** and **52**, the noise equivalent bandwidth, needed for evaluating photon noise, is evaluated as

$$\Delta f = \frac{\int_0^{\infty} \left|Z_T(2\pi i f)\right|^2 df}{\left|Z_{T_{\max}}\right|^2} \quad [\mathrm{Hz}]. \tag{60}$$

### 2.2.D. Pulse detection in the presence of noise

If the transmitted signal is pulsed (with effective pulse width $\tau_x$) and the receiver is temporally windowed (effective gate width $\tau_r$), the signal to noise ratio of **Equation 39** becomes ($NEI_s$ removed from $NEI_{ph}$)

$$SNR_{detection} = \frac{\Phi_s \cdot \tau_x}{\sqrt{NEI_s^2 \cdot \tau_x^2 + \left(NEI_{ph}^2 + NEI_{dar}^2 + NEI_{sys}^2\right)\cdot \tau_r^2}} \quad [\text{ph-m}^{-2}/\text{ph-m}^{-2}]\,, \tag{61}$$

where it has been assumed that $\tau_r \geq \tau_x$. Note that $SNR_{detection}$ is maximized when the receiver is temporally matched to the transmitted pulse, i.e. $\tau_x \approx \tau_r$. This pseudo matched-filter condition is best understood through a review of matched filter[44] detection. To detect a signal, *s(t)*, in the presence of noise, *n(t)*, the receivers electronic impulse response, *h(t)*, is selected to maximize the detection signal to noise ratio. *h(t)* maximizes the signal to noise ratio

$$SNR = \frac{s(t) * h(t)}{\sqrt{n(t) * h(t)}}, \tag{62}$$

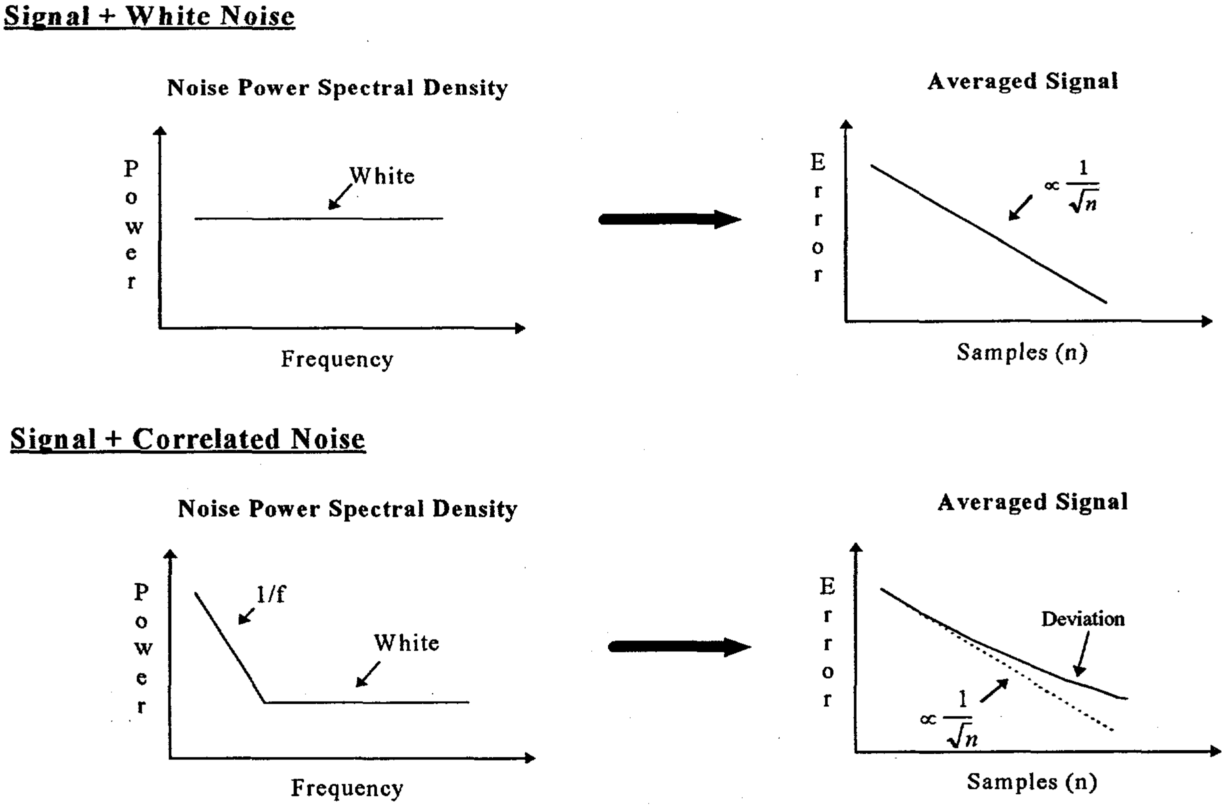

**Figure 11.** Illustration of Potential Degradation of Multi-Sample Averaged Signal Error Due to Correlated Noise.

when the condition that the receiver response equal the conjugate signal, or $h(t) = s^*(t)$, is satisfied. Realistically, a true matched filter is difficult to implement in practice, hence, a pseudo matched-filter, $h(t) \approx s(t)$, is constructed to provide near matched filter performance. It should be noted that the transmitted laser pulse can temporally fluctuate on a shot-to-shot or line-to-line basis, and in an elevated platform narrow pulses can broaden depending on terrain profile and angular incidence. The receiver, and hence, matched filter will have to track these fluctuations.

One final note on receiver sensitivity, once $NEI_{tot}$ is known, the minimum receiver sensitivity (SNR $\approx$ 1) can be estimated with

$$P_{\min} = NEP_{receiver} = \frac{h\cdot c}{\lambda_o}\cdot\frac{A_d}{\eta_r\cdot\left(1-\left(\frac{D_{r\_obs}}{D_r}\right)^2\right)}\cdot NEI_{tot} \qquad (63)$$

where $P_{min}$ is the minimum detectable rms power in watts at the receiver aperture, $\lambda_o$ is the optical center wavelength, $A_d$ is the detector's active optical area, $\eta_r$ the receiver optical efficiency, and $D_r$, $D_{r\_obs}$ are the receiver aperture diameter and aperture obstruction, respectively.

### 2.2.E. Correlated noise and system performance

Correlated noise, in a practical sense, is noise whose distinguishing characteristics include a varying power spectral density over the frequency range of interest and, conversely, a broadening of its autocorrelation function (over the temporal range of interest). The primary degrading effect of correlated noise on DIAL is the potential of a reduction in multi-sample averaging efficiencies[45] ( non-√n noise convergence). A simplified illustration of the relationship between correlated noise and degradation in averaging efficiencies is shown in **Figure 11**. If a signal of constant amplitude is detected in the presence of white noise (noise spectral density is flat), the improvement in the standard deviation of the signal-to-noise ratio follows a square root progression when averaged over n-samples. If a signal of constant amplitude is detected in the presence of correlated noise (in this case one-over-frequency (1/f) and white noise), the improvement in the standard deviation of the signal-to-noise ratio may deviate from the square root progression when averaged over n-samples. The typical sources of correlated noise in DIAL include non-random fluctuations in transmitter (temporal, spectral and spatial), receiver (detector and electronics),[46] transmitter/receiver geometric form factor fluctuations, atmosphere[47] and target statistics (speckle, albedo and plume dynamics). The most commonly encountered, and most widely studied, correlated noise is 1/f noise. Low-frequency 1/f noise is a class of noise that is widespread in nature, and whose noise spectral density follows a $1/f^{\beta}$ distribution (typically $0.5 \leq \beta \leq 2$).[48, 49] Since multi-shot averaging is required in most DIAL applications, *controlling correlated noise sources in DIAL receiver systems is essential for maximum multi-sample averaging efficiency.*

## 3. DESIGN EXAMPLE: A SINGLE-ELEMENT DIAL RECEIVER

### 3.1. Summary of Performance Requirements

The best way to initiate a robust system design is by first scripting a precise statement of the performance requirements followed by a concise system synthesis prescription that clearly relates performance requirements to synthesis requirements. The design methodology of a DIAL receiver system should be no less robust – a clear definition of the performance requirements and synthesis requirements is an essential first step in the design process. Simply stated, the requirements are to build a receiver for a 10 to 100 kHz pulse repetition rate (PRR) laser with a 100 ns to 500 ns single-shot pulse width (Gaussian waveform, 1/e to 1/e width) at a minimum energy of 250 μJs per pulse. The system will be pseudo-coaxial (outgoing beam is coaxially steered with receiver's obstruction) with a maximum range of 10 km. Due to variations in range and terrain profile, the receiver is required to detect both the magnitude and time of flight (TOF) of the laser's return pulse. The receiver detector/amplifier noise is expected to equal the background photon noise given an optical bandwidth of 8.5 to 11.5 μm (50% transmission points), and a receiver-FOV to transmitter-divergence product that yields a single-shot speckle SNR of approximately 10 at the 10 km range. In addition, multi-shot averaging will be employed and correlated noise sources must be suppressed or minimized.

### 3.2.A. Summary of Synthesis Requirements

In derivation of the receiver synthesis requirements, the following system trade issues are to be considered:

- active detector area ↔ detection noise,
- active detector area ↔ receiver FOV or receiver TSD diameter at target, $D_{rt}$, (minimum effective receiver F# of approximately unity assumed),
- $D_{rt}$, ↔ effective beam diameter at target, $D_{xt}$,
- $D_{rt}$, $D_{xt}$ ↔ speckle SNR,
- $D_{rt}$, $D_{xt}$, ↔ geometric form factor (GFF) and GFF modulation,
- $D_{rt}$, $D_{xt}$, ↔ receiver resolution and laser divergence limitations,
- $D_{rt}$, $D_{xt}$, ↔ target acquisition and sensitivity requirements (see Appendix A for estimating sensitivity requirements).

Employing the analysis tools described in **Section 2**, an iterated, self consistent solution that optimizes the above trade issues given the stated performance requirements results in the following synthesis requirements.

**Simulation Parameters Assumed in Optimization Study:**

- Wavelength: $\lambda_o = 10.6$ μm
- Range: $R = 10$ km
- Atmospheric transmission @ range $R$: $T_a = 0.5$
- Atmospheric structure factor: $C_n^2 = 5 \cdot 10^{-15}$ m$^{-2/3}$

- Target reflectivity at normal incidence: $\rho = 3\%$

**Transmitter Requirements:**

- Beam diameter @ transmitter: $D_x = 0.1$ m
- Effective beam divergence and beam diameter at range: $\theta_x = 2.5\cdot10^{-4}$ radians, $D_{xt} = 2.6$ m
- Spatial profile: Clipped Gaussian ($\alpha = \sqrt{2}$)
- Temporal profile: Gaussian with 1/e pulsewidth = 100 ns
- Nominal energy: 250 μJ
- Optical transmission efficiency: $\eta_x = 0.75$

**Receiver Requirements:**

- Clear aperture diameter: $D_r = 0.40$ m
- Obstruction diameter: $D_{r\_obs} = 0.15$ m
- Aperture to obstruction distance: $Z_{r\_obs} \sim 0.5$ m
- Effective receiver focal length: $f_l = 0.40$ m (resulting in an F# = 1 system)
- FOV: $\theta_r = 5\cdot10^{-4}$ radians
- Active detector diameter: $D_d = 200$ μm
- Resolved field @ range: $D_{rt} = 5.4$ m
- Optical bandwidth: 8.5 to 11.5 μm
- Optical train and filter transmissions: $T_o = 0.75$ and $T_f = 0.9$
- Active detector quantum efficiency: $\eta_d = 0.85$
- Effective optical train temperature and emissivity: $T_{op} = 300$ K $\varepsilon_{op} = 0.05$
- Field-Stop temperature and emissivity: $T_{fs} = 300$ K $\varepsilon_{fs} = 0.9$
- Cold-Shield temperature, emissivity and FOV: $T_{cs} = 77$ K $\varepsilon_{cs} = 0.99$ $FOV_{cs} = 60$ degrees
- Optical defocus tolerance: $\Delta_{fs} = \pm 30$ μm
- Optical aberration tolerance: $\Delta_{ab} = 5\cdot10^{4}$ cycles/m
- Noise equivalent bandwidth assuming pseudo-matched filter detection of a 100 ns Gaussian pulse: $\Delta f = 4$ MHz
- Total background, optics and cold-shield photon noise NEP (NEI) budget referenced at detector: $\text{NEP}_{\text{ph}} = 0.3$ nW ($\text{NEI}_{\text{ph}} = 4\cdot10^{17}$ ph/m$^2$-s)
- Total detector, amplifier and readout NEP (NEI) budget referenced at detector: $\text{NEP}_{\text{dar}} = \text{NEP}_{\text{ph}} = 0.3$ nW ($\text{NEI}_{\text{dar}} = 4\cdot10^{17}$ ph/m$^2$-s)

**Joint Transmitter/Receiver Requirements:**

- Relative transmitter/receiver alignment LOS tolerance: $\zeta \leq 5\cdot10^{-5}$ radians
- Geometric form factor and resolution efficiency @ range: $\xi_{xr} = 0.97$, $\xi_{res} = 0.94$, with $\xi_{xr}\cdot\xi_{res} = 0.92$

### 3.2.B. Summary of Projected System Performance

The synthesis parameters listed above will result in the single-shot, speckle, detection and composite SNR plotted in **Figure 12** as a function of range. Note that at $R = 10$ km, both speckle and detection noise produce approximately equal signal SNR. This is a ramification of optimizing speckle noise and detection noise by adjusting the active detection area given a system F# ≈ 1 while simultaneously maximizing high geometric form factor and resolution efficiencies. For most applications, designing for $SNR_{speckle} \approx SNR_{detection}$ leads to optimal system performance. The relationship between the composite SNR and first-order DIAL system sensitivity requirements is given in **Appendix A** for single and multi-line-pair samples.

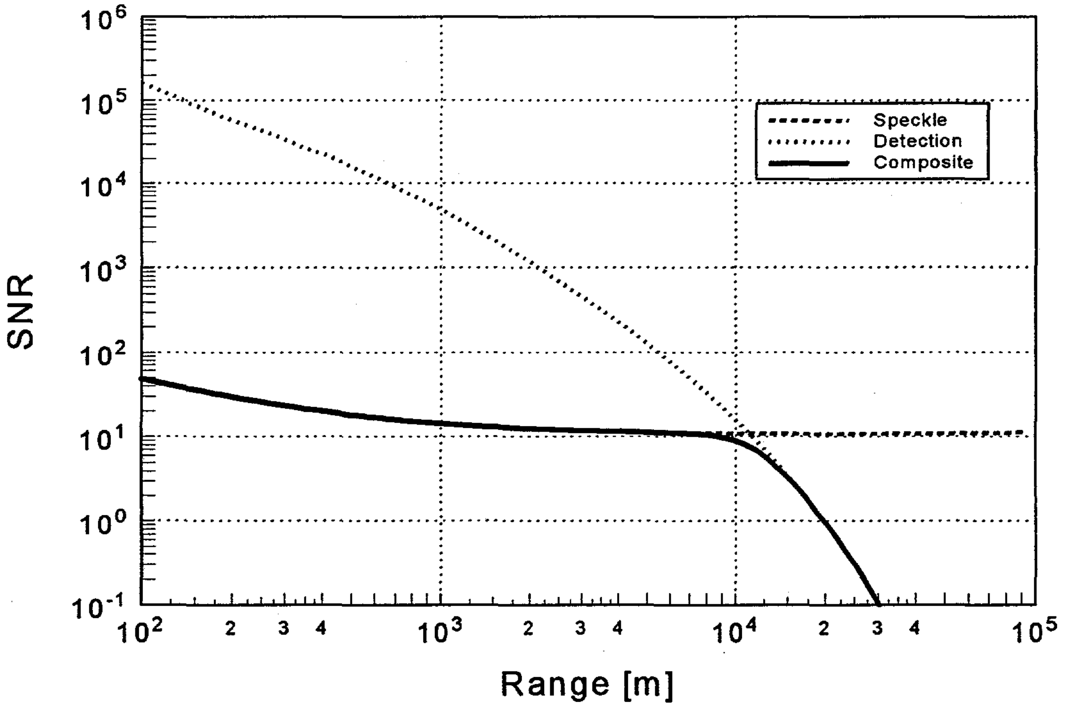

**Figure 12.** Projected Single-Shot System Performance: Speckle, Detector and Composite (Total) SNR vs. Range.

### 3.3. Receiver Design Summary

A summary of the detection system (detector, amplifier and readout) and dewar system follow.

### 3.3.A. Detection System

A summary of the primary technical design objectives listed in the receiver synthesis requirements outlined in Section 3.2.A. includes:

- measure returned signal power (magnitude) of the 100 ns, Gaussian return pulse at a 10 - 100 kHz PRR, and,
- provide real-time temporal or time-of-flight (TOF) tracking of the return pulse,
- limit detector, amplifier and readout noise to $NEP_{dar} = 0.3$ nW or $NEI_{dar} = 4 \cdot 10^{17}$ ph/m$^2$-s ,
- remove or minimize drift and correlated noise.

A block diagram of the prototype detection system is depicted in Figure 13. An optical pulse, incident upon the detector, is converted to an electrical signal, amplified and filtered by h(t). The filter h(t) is selected such that the overall electronic detection response is closely matched to the optical pulse (pseudo-matched filter) for near optimal detection. Pulse magnitude is detected via gated peak detection or integration, while a discriminator detects the temporal time-of-flight. Photon noise is minimized through cold shielding and optical filtering, while drift is stabilized with active baseline restoration.

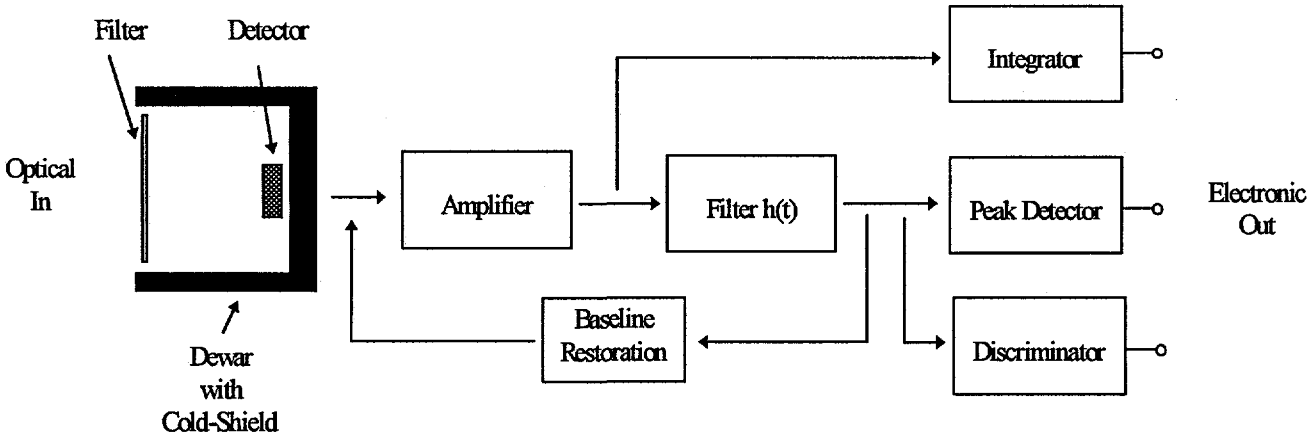

**Figure 13.** Prototype Detection System.

### 3.3.A.1. Detector and amplifier electronics

For convenience, output noise equations **Eq. 55 - 57 of Section 2.2.C.2.** (simplified with $A(f) \rightarrow \infty$ and $R_s \rightarrow 0$) are restated as a reference for what follows:

$$v_{n\_o}(f) = \sqrt{\left[ v_n^2(f) \left| 1 + \frac{R_f}{\frac{R_d\, R_a}{R_d + R_a}} \frac{1 + 2\,\pi\, i\, f\, \frac{R_d\, R_a}{R_d + R_a}\left(C_d + C_a\right)}{1 + 2\,\pi\, i\, f\, R_f\, C_f} \right|^2 + i_n^2(f) \left| \frac{R_f}{1 + 2\,\pi\, i\, f\, R_f\, C_f} \right|^2 \right] \left| H(2\pi i f) \right|^2} \qquad (55)$$

with the input referenced voltage and current noise density

$$v_n(f) = \sqrt{\left( v_{n\_a} \left( 1 + \frac{1}{f} f_{v\_1/f\_a} \right) \right)^2} \quad [\mathrm{V}/\sqrt{\mathrm{Hz}}], \text{ and} \qquad (56)$$

$$i_n(f) = \sqrt{\left( 2\, q \left( I_d + I_p \right) + \frac{4\, k\, T}{R_d} + \frac{k_{1/f\_d}^2\, I_d^2}{f} \right) \left| \frac{R_d}{R_d + 2\pi i f} \right|^2 + \frac{4\, k\, T_a}{\frac{R_f\, R_a}{R_f + R_a}} + \left( i_{n\_a} \left( 1 + \frac{1}{f} f_{i\_1/f\_a} \right) \right)^2} \quad [\mathrm{A}/\sqrt{\mathrm{Hz}}]. \qquad (57)$$

Referring to **Equations 55 - 57**, the following general observations concerning noise reduction can be offered:

- $R_f$, $R_d$, and $R_a$ → very large
- $C_f$, $C_d$, and $C_a$ → very small,
- $R_f C_f$ time constant → much less than $1/\mathrm{PRR}_{\max}$,
- detector dark current, $I_d$ → small (note background photocurrent, $I_p$, was fixed during synthesis requirements),
- amplifier input voltage and noise current $v_{n\_a}$ and $i_{n\_a}$ → small,
- filter $H(s)$ → matched to signal bandwidth.

As it happens, optimization of the detection electronics in a single-element receiver begins with specifying the active detector area. Without full consideration of system requirements, one could specify a tiny detector with vanishing capacitance and high impedance, and build a near-noiseless receiver. Unfortunately, so as to meet practical receiver FOV

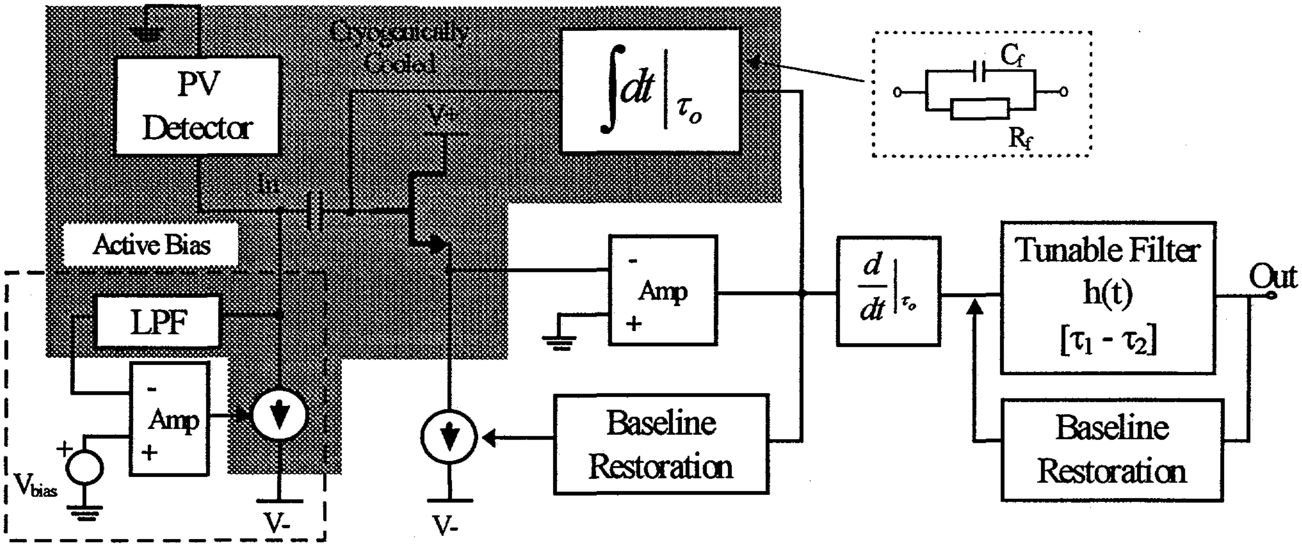

**Figure 14.** Block Diagram of Detection Electronics Synthesis.

requirements, speckle SNR, and GFF/resolution/alignment requirements (see **Section 3.2.A.**), a single-element receiver will normally require an appreciable active-detector area, leading to nominal amounts of detector capacitance, $C_d$, and reduced detector dynamic impedance, $R_d$. Combined with the potentially high temporal bandwidth requirements of narrow pulse detection, the design of low-noise detection electronics can rapidly become a nontrivial issue. Our approach at a high bandwidth, low noise design is illustrated in **Figure 14**. The amplifier topology is transimpedance with the following features.

- A pole-zero (integrate-derivative) cancellation approach is implemented where $R_f$ is made very large reducing the noise floor. However, an integrator (pole) is formed with $C_f$, producing an integration time-constant of $\tau_o = R_f C_f$ thereby limiting the bandwidth to $1/2\pi\tau_o$. This loss in bandwidth is then restored through a derivative (zero) operation with a time constant of $\tau_o$. Hence, the reduced noise advantage of a large $R_f$ can be preserved without loss of bandwidth (note that all DC information is lost - not a problem with pulse detection).
- A cooled (~100K), low-noise input field effect transistor (FET) for reduced $v_{n\_a}$ and $i_{n\_a}$.
- The FET and all circuit elements connected to the detector are placed in a dewar in close proximity to the detector and cooled for low noise performance.
- An active photovoltaic bias circuit for minimum drift, rapid transient recovery, and low noise.
- An active baseline restoration that tracks and reduces baseline drift and improves correlated noise rejection.
- A tunable electronic filter, h(t), for pseudo-matched filter detection of 100 to 500 ns pulses.

The electronic filter, h(t), is selected so as to closely match receiver to signal bandwidth, optimizing the signal to noise performance. The Fourier transform pair and noise equivalent bandwidth (**Equation 41**) of a temporal Gaussian pulse, 1/e to 1/e pulse width = $\tau_g$, is given by[50]

$$\frac{1}{\sqrt{2\pi\sigma^2}}\, e^{-\frac{t^2}{2\sigma^2}} \Leftrightarrow e^{-2\pi^2\sigma^2 f^2}, \quad \sigma = \frac{\tau_g}{2\sqrt{2}}, \tag{64}$$

$$\text{and } \Delta f = \frac{1}{\sqrt{2}\,\pi\,\tau_g}. \tag{65}$$

Note that in addition to being used in photon noise calculations, Δf is also a practical performance measure for pseudo-matched filter optimization due to its preferential weighting of high frequencies. The simplest electronic filter available is the n-stage cascade of 1st order low pass filter with a transform pair given by

$$\frac{t^{n-1}}{(n-1)!} e^{-\frac{t}{\tau}} \Leftrightarrow \frac{\left(\frac{1}{\tau}\right)^n}{\left(2 \pi i f + \frac{1}{\tau}\right)^n} , \tag{66}$$

where $\tau$ is the single-stage, 1st order low pass filter's time constant. Currently, the relations given in **Section 2.2.C.2** or a SPICE based circuit simulator are used to select, through iteration, the optimal values of $n$ and $\tau$ for a given laser pulse. **Section 3.3.C.** tabulates the optimal $\tau$, the NEP/NEI and $\Delta f$ for 100 ns, 250 ns, and 500 ns Gaussian pulses given n =5.

### 3.3.A.2. Detector Characteristics

A $Hg_{1-x}Cd_xTe$ photovoltaic detector with a very high $R_d$ and low $I_d$ is essential if the noise levels dictated by the synthesis requirements are to be meet. The detector is a Double Layer Heterojunction (DLHJ) photovoltaic LWIR $Hg_{1-x}Cd_xTe$ detector with an anti-reflection coating tuned for approximately 11.5µm. The DLHJ detector is fabricated utilizing a mercury rich liquid phase epitaxial process developed at Santa Barbara Research Center. The detector cutoff was originally set by adjusting the ratio of HgTe to CdTe such that a cutoff of approximately 10.8µm was obtained at the 75 K operating temperature. The wavelength of these devices can be further extended by reducing the temperature and taking advantage of the reduction in energy gap of HgCdTe that comes with lower temperatures as shown in **Figure 15**.

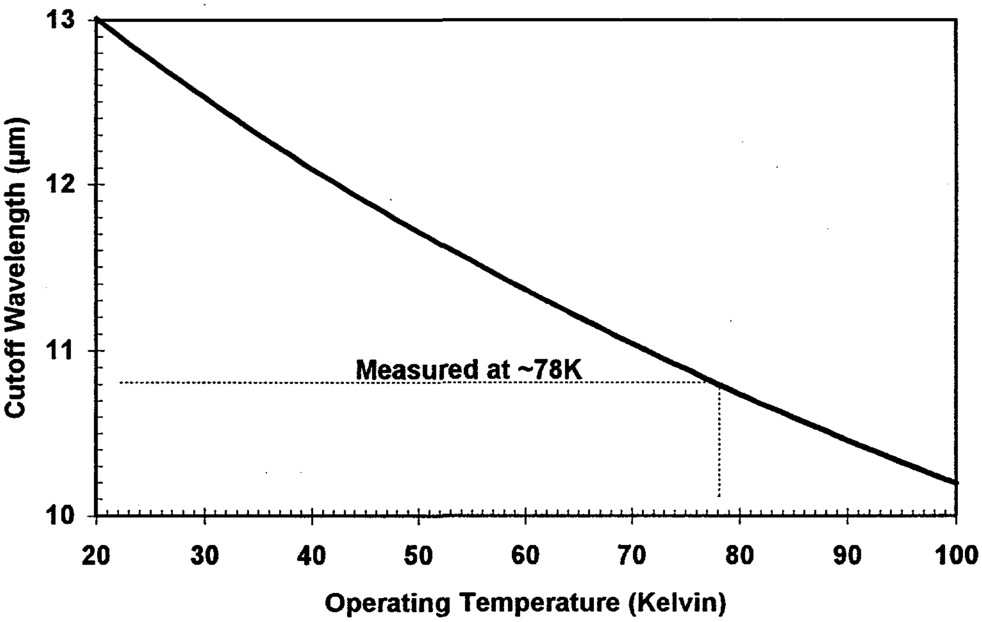

**Figure 15.** The Cutoff Wavelength of HgCdTe Increases With Temperature. The Device Has a Cutoff of ~10.8µm at 78K and Should be Cooled to Less than ~40K for Performance Beyond 12µm. The equation used is from Seiler, et. Al. (Journal of Vacuum Science Technology, Vol. 8, No. 2, March/April 1990).

The actual detector utilized is one of many devices provided on the Test Structure Assembly (TSA) in both single element and small array formats. Single element mesa detectors include sizes ranging from 30 to 800 microns square. This instrument utilizes detector V07, one of two 200µm single element mesa detectors available on the TSA die. It should be noted that the actual effective optical area of the detector is slightly larger due to the approximate 10µm minority carrier lateral collection. These single element detectors are not gated and do not include guard structures surrounding the photo

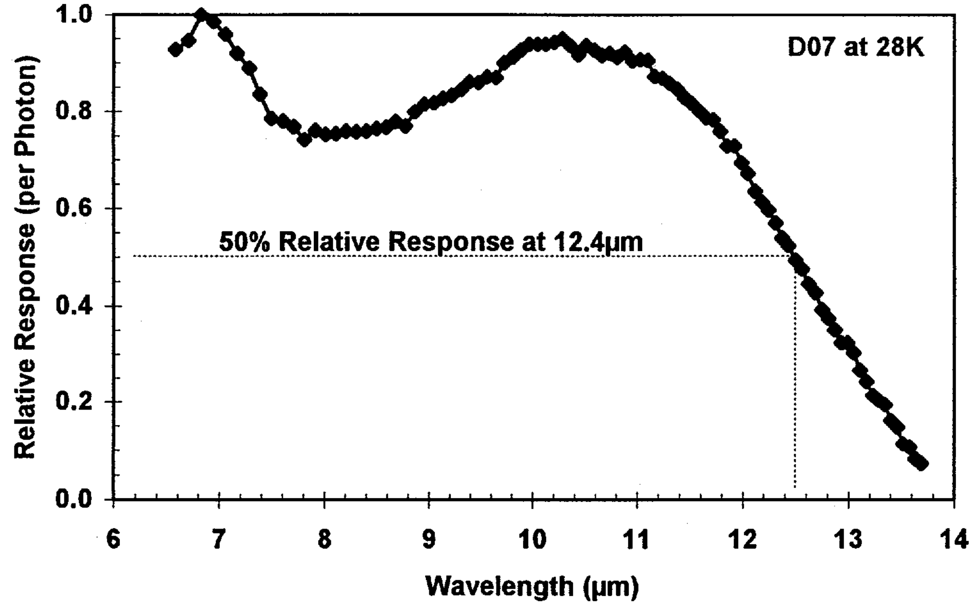

**Figure 16.** Relative Photon Flux for the Anti-Reflection Coated Detector Shows the Desired Peak in Response in the Region of 11 μm. The Cutoff is Estimated to be ~ 12.4 μm at the 28 Kelvin Temperature at Which These Data Were Collected.

sensitive area. The detector response versus wavelength is shown in **Figure 16**. Note, a narrow band AR coating has been utilized in lieu of a broadband coating that would have compromised peak response at the longer wavelengths. Since the laser detection system effectively filters out-of-band energy, there was no desire to trade peak response for wide band response. The absolute peak response, at 7μm, is greater than 95% absolute. The scale shown in the figure is relative, normalized to the peak. The response of the detector at 11.5μm is approximately 80% of the peak response.

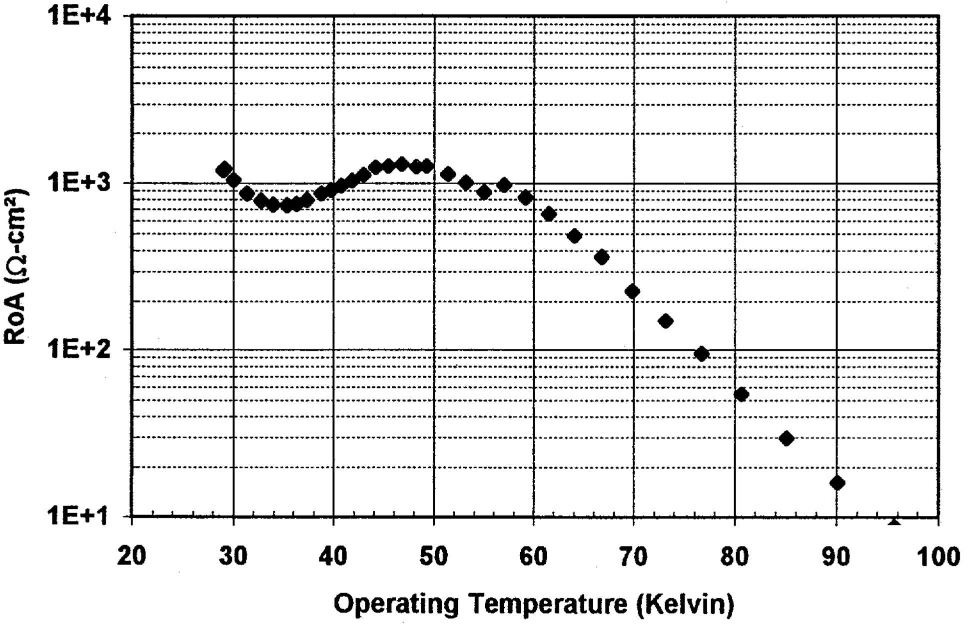

**Figure 17.** RoA Versus Temperature Indicates ~1,000 Ω-cm² Below ~60 Kelvin. Test Equipment Limits May be Limiting the RoA at Lower Temperatures.

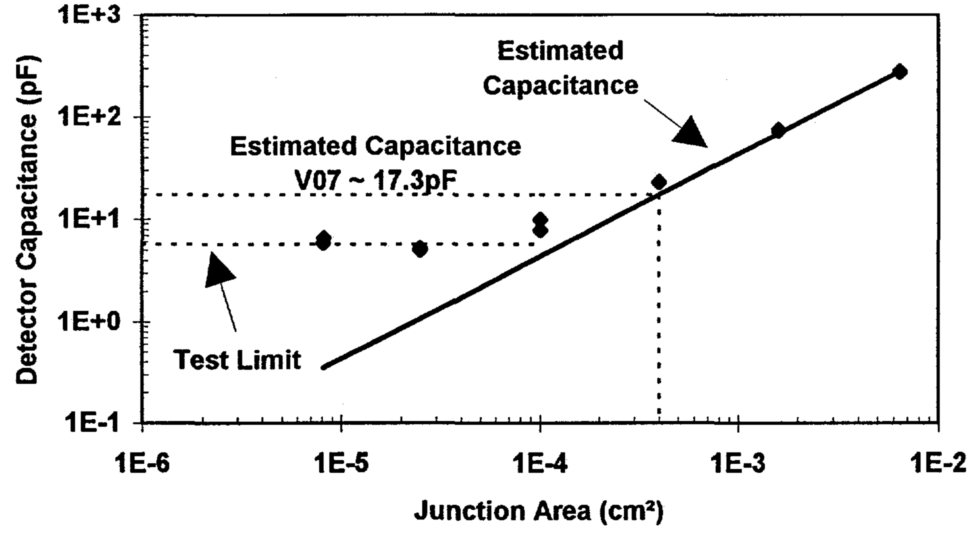

**Figure 18.** Capacitance of Detectors of Various Sizes are Measured to Determine the Capacitance Per Unit Area of the Junction After Removal of Stray Test Equipment Capacitance.

High detector impedance provides the system with both low noise and low dark current. The resistance-area product at zero bias (RoA) is approximately 1,000Ω-cm² for temperatures below 60 Kelvin. RoA versus temperature is shown in **Figure 17**. The leveling off of RoA at temperatures below 55 Kelvin has not been fully investigated, but may be instrument related (such as high background flux) or detector limited (tunneling). Higher RoA product measured at Los Alamos National Laboratories (not shown) suggest test equipment limits.

Detector drift was measured in the form of 1/f noise for detector V07. The noise corner is below 10 Hz. More typical detectors have a noise corner (the frequency at which the white noise intercepts the 1/f noise) less than 3Hz and many are well below 1Hz. 1/f noise is difficult to test as the procedure often measures the drift in the dewar cold shield temperature as well as actual detector dark current drift.

Capacitance on the preamplifier input increases the total noise of the instrument by "boosting" or gaining up the white noise of the JFET preamplifier at higher frequencies. Detector capacitance is the primary contributor to the capacitance on the input. The detector capacitance, estimated to be about 17pF, was measured on devices fabricated in the same lot and is plotted as a function of detector area on **Figure 18**.

### 3.3.B. Dewar

The two primary dewar requirements are a 60° detector FOV, and to achieve the 12 μm cutoff, the detector must be cooled to 35 K. The dewar manufacturer, IRL *(Infrared Laboratories Inc.*, Tucson, Arizona), modified one of their existing designs to meet requirements. Briefly, the dewar is a cylindrical-shaped, IRL HDL-8 series dewar (8 inch cold plate) with nitrogen and helium reservoirs, a six position cooled filter wheel, 3-inch zinc selenide window and the universal fanout board and socket. It is unusual, in that its large window had to be mounted on one of the circular end plates, so it is operated lying on its side and is filled through ports on the end plate opposite the windowed plate. In this configuration, the detector can be held at 35 K, and the amplifier at 100 K for five to six hours.

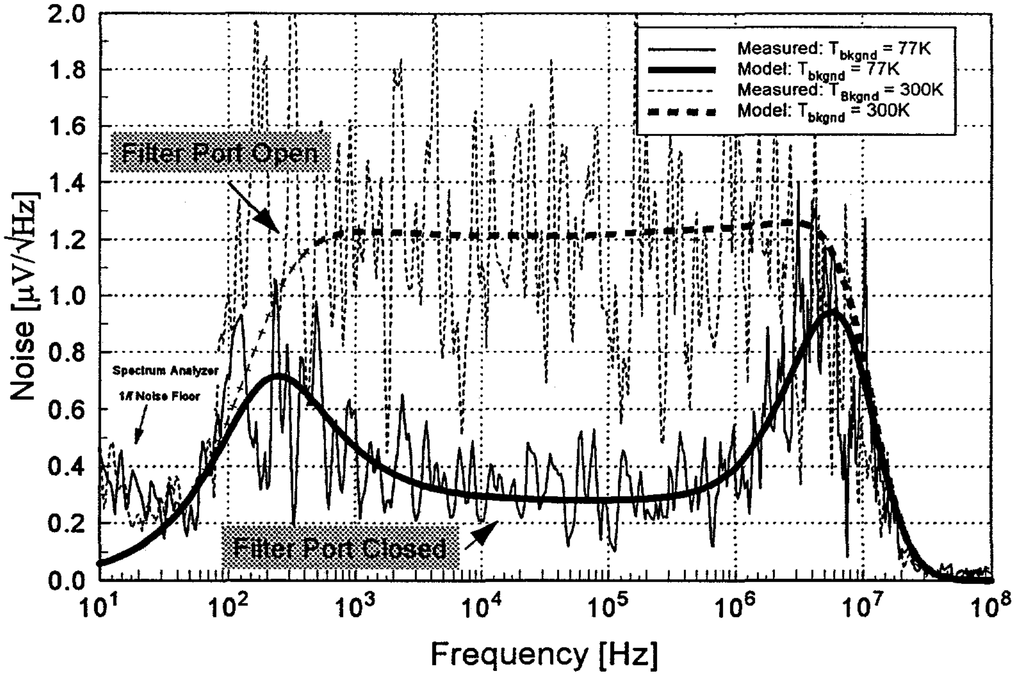

**Figure 19.A.** Measured and Modeled Receiver Output-Referenced Noise Spectral Density: Optical Filter Port Closed ($T_{bkgnd}$ = 77K), and 8.5 - 11.5 µm Filter Port Open ($T_{bkgnd} \sim 300K \rightarrow I_p \sim 5$ µA). The Receiver FOV, Responsivity, and Amplifier Transimpedance Gain are 60°, $6.8 \cdot 10^6$ V/W, and $10^6$ V/A Respectively.

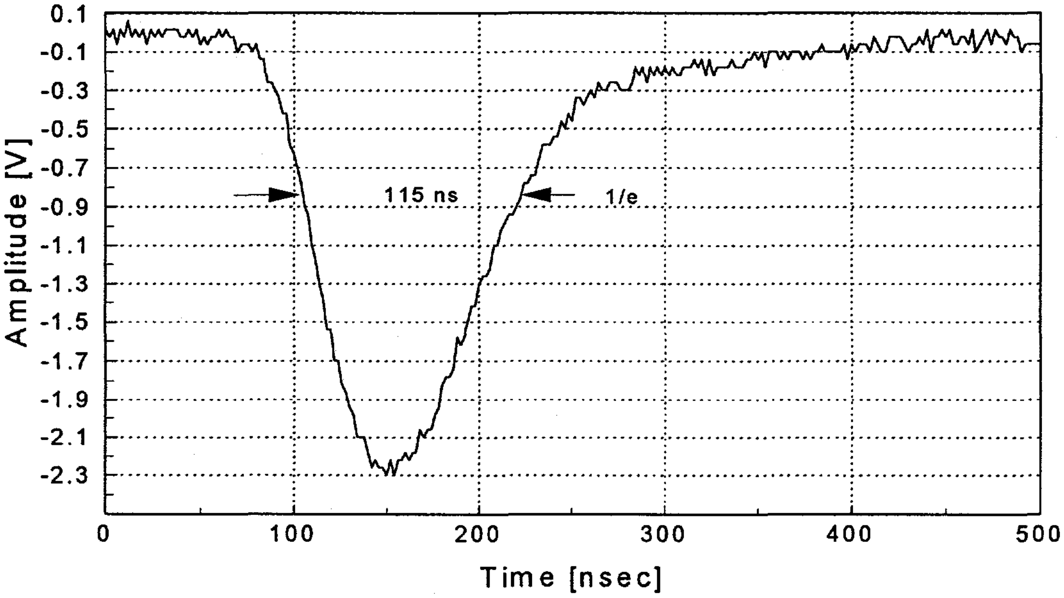

**Figure 19.B.** Receiver Transient Response to 20 - 25 nsec YAG Pulse. The Response Width is Enlarged due to the Broad YAG Pulse.

### 3.3.C. Modeling and Experimental Measurements

The resulting detector/amplifier parameters (see **Section 2.2.C.2.**) that model the prototype follow:

*Note - all detector parameters given at 35 K and 50 mV reverse bias, $R_a$ = effective resistance of active bias circuit, h(t) is the 5th order filter described by* ***Equation 66*** *(n = 5 and $\tau = \tau_2$).*

$A_d$ [m$^2$]: $(200 \cdot 10^{-6})^2$
$I_d$ [A]: $< 10^{-9}$
$GB$ [Hz]: $200 \cdot 10^6$
$R_f$ [Ω]: 1 M
$i_{n\_a}$ [A/√Hz]: $0.25 \cdot 10^{-25}$

$R_d$ [Ω]: 4 M
$I_p$ [A]: 0 or $\sim 5 \cdot 10^{-6}$
$f_a$ [Hz]: 100
$C_f$ [F]: $1 \cdot 10^{-12}$
$f_{i\_1/f\_a}$ [Hz]: $1 \cdot 10^3$

$R_s$ [Ω]: 25
$k_{1/f\_d}$ []: $1 \cdot 10^{-6}$
$R_a$ [Ω]: 300 K
$v_{n\_a}$ [V/√Hz]: $1.55 \cdot 10^{-9}$
$T_a$ [K]: 100

$C_d$ [F]: $17.5 \cdot 10^{-12}$
$T_d$ [K]: 35
$C_a$ [F]: $12.5 \cdot 10^{-12}$
$f_{v\_1/f\_a}$ [Hz]: $1 \cdot 10^3$

$$H(f) = G\left(\frac{2\pi i f}{2\pi i f + 2\pi f_{hp}}\right)^2 \frac{2\pi i f + \frac{1}{\tau_1}}{2\pi i f + \frac{1}{\tau_1} + \frac{1}{\tau_2}} \left(\frac{\frac{1}{\tau_2}}{2\pi i f + \frac{1}{\tau_2}}\right)^4$$

$G$ [V/V] = gain constant
$f_{hp}$ [Hz] = 200
$\tau_1$ [sec] = $R_f \cdot C_f$
$\tau_2$ [sec] = $\varepsilon \cdot \tau_1$

The modeled ($G$ =100, $\varepsilon$ = .0094, $\tau_2$ = 9.4 ns) and measured receiver output-referenced, noise spectral density into 1M Ω load, and measured pulse response (to an 20 - 25 nsec YAG pulse) are shown in **Figures 19.A** and **19.B**. The noise spectral density plots show the detector/amplifier noise (optical filter port closed, $T_{bkgnd}$ = 77K), and that of the detector/amplifier + background noise (8.5 - 11.5 μm filter port open, $T_{bkgnd} \sim$ 300K → $I_p \sim$ 5μA). The receiver FOV, responsivity, and amplifier transimpedance gain are 60°, $6.8 \cdot 10^6$ V/W @ 10.6 μm, and $10^6$ V/A respectively. The setting $\tau_2$ = 9.4 ns, which is approximately half the smallest time constant anticipated, maximizes the useful amplifier bandwidth at a transimpedance gain of $1 \cdot 10^6$ V/A (the 200 MHz amplifier gain-bandwidth product becomes the limit) and provides the worst-case, detection noise baseline that is used to calibrate the noise-model parameters (see **Figure 19.A**). With the calibrated noise parameters, the detection noise for 100, 250 and 500 ns Gaussian pulses is evaluated and listed in **Table 1**. The values of $\tau_2$ (n = 5) are selected so as to provide near matched filter response for 100, 250 and 500 ns pulses. It should be emphasized that the pseudo-matched filter approach discussed in this section is grounded on the recognition that DIAL measurements require detection of the return pulse *magnitude* (as opposed to the complete waveform), and that temporal time-of -flight can be estimated by the previous time-of -flight measurements.

**Table 1.** Detection Noise for 100, 250 and 500 ns Gaussian Pulses.

| Pulse Width $\tau_g$ [ns] | $\tau_2$ [ns] | $\Delta f_{pulse}$ [MHz] | $\Delta f_{receiver}$ [MHz] | $NEP_{dar}$ [nW] | $NEI_{dar}$ [ph/m$^2$-s] |
|---|---|---|---|---|---|
| 100 | 15 | 3.99 | 3.86 | 0.272 | $3.63 \cdot 10^{17}$ |
| 250 | 42 | 1.60 | 1.67 | 0.090 | $1.20 \cdot 10^{17}$ |
| 500 | 88 | 0.80 | 0.83 | 0.046 | $6.09 \cdot 10^{16}$ |
| - | 9.4 | - | 5.16 | 0.428 | $5.71 \cdot 10^{17}$ |

Note with a nominal background noise level of ~ 0.27 nW (300K background), the receiver is near or below the background limit for detected pulse 100 ns or longer.

## 4. CONCLUSION

Based on our current understanding of the receiver/transmitter noise processes, we have developed an analysis methodology and corresponding analytical tools for the design of optimized low-noise, hard target return $CO_2$ DIAL receiver systems implementing both single element detectors and multi-pixel imaging arrays for passive/active, remote-sensing applications. In addition, experimental results for a developmental single-element detector receiver designed to detect 100 ns wide laser pulses (10-100 kHz pulse repetition rates) backscattered from hard-targets at nominal ranges of 10 km were presented. The receiver sensitivity is near-background noise limited, given a 8.5-11.5 μm radiant optical bandwidth, with the total noise floor spectrally white for maximum pulse averaging efficiency.

## APPENDIX A: ESTIMATING DIAL SENSITIVITY REQUIREMENTS

In the following, a simplified approach allowing first-order estimations of DIAL sensitivity requirements is provided. An example follows relating the sensitivity requirements to DIAL signal-to-noise ratios (SNR) for single and multi-line-pair samples. Defining the normalized differential sensitivity of the return DIAL Reference and Probe power as

$$\Delta P_n = \frac{P_{ref} - P_{probe}}{P_{ref}},$$

where the assumption that $P_{ref} \approx P_{probe}$ and $P_{ref} \geq P_{probe}$ has been made, the first order linear and log DIAL measurement sensitivities (derived from absorption relations defined in Measures, see Ref. 1) are given by:

$$S_{lin} = \Delta P_n^{-1} \approx \left[1 - e^{-2\cdot\Delta\alpha\cdot PPX\cdot t\cdot\xi}\right]^{-1} \approx \frac{1}{2\cdot\Delta\alpha\cdot PPX\cdot t\cdot\xi}, \qquad 2\cdot\Delta\alpha\cdot PPX\cdot t\cdot\xi \quad << \quad 1,$$

$$S_{log} = \left[\ln(\Delta P_n)\right]^{-1} \approx \left[\ln\left(1 - e^{-2\cdot\Delta\alpha\cdot PPX\cdot t\cdot\xi}\right)\right]^{-1} \approx \frac{1}{2\cdot\Delta\alpha\cdot PPX\cdot t\cdot\xi}, \qquad 2\cdot\Delta\alpha\cdot PPX\cdot t\cdot\xi \quad << \quad 1,$$

where

$\Delta\alpha$ = target species differential absorption [$m^{-1}$ atm],
$PPX$ = desired resolution in parts-per-x (x = million, billion etc) [$atm^{-1}$],
t = thickness of target species layer [m],
$\xi$ = estimate of target/transceiver overlap efficiency [0-1].

Note that the above sensitivity definitions assume near perfect differential cancellation and hence represents an upper bound on the DIAL measurement.

As an example, if $\Delta\alpha$ = 1000 [$m^{-1}$ atm], $PPX$ = 1 PPM [$atm^{-1}$], t = 1 meter and ξ =,1 then the linear sensitivity function evaluates to $S$ = 500 implying an aggregate measurement sensitivity requirement of at least 1 part in 500 for a 1 PPM resolution. Furthermore, assuming a single-shot SNR of 5, then at least $(500/5)^2$ = 10,000 decorrelated line-pair samples are needed for a 1 PPM resolution. As described in **Section 2.2.E.**, statistically correlated samples will increase the number of required line-pair samples.

# REFERENCES

---

[1] R. M. Measures, *Laser Remote Chemical Analysis*, John Wiley & Sons, 1988.

[2] A. Papoulis, *Probability, Random Variables and Stochastic Processes*, McGraw-Hill, 1984.

[3] J. Harms, "Lidar return signals for coaxial and noncoaxial systems with central obstructions," *Applied Optics*, Vol. 18(10), pp. 1559-1566, May 1979.

[4] T. Halldorsson, and J. Langerholc, "Geometrical form factors for the lidar function," *Applied Optics*, Vol. 17(2), pp. 240-244, January 1978.

[5] J. Harms, W. Lahmann, and C. Weitkamp, "Geometrical compression of lidar return signals," *Applied Optics*, Vol. 17(7), pp. 1131-1135, April 1978.

[6] J. W. Goodman, *Introduction to Fourier Optics*, McGraw-Hill, 1968.

[7] R. G. Wilson, *Fourier Series and Optical Transform Techniques in Contemporary Optics*, John Wiley & Sons, 1995.

[8] J. W. Goodman, *Statistical Optics*, John Wiley & Sons, pp. 374-384, 1985.

[9] G. O. Reynolds, J. B. DeVelis, G. B. Parrent Jr., B. J. Thompson, *The New Physical Optics Notebook: Tutorials in Fourier Optics*, SPIE Optical Engineering Press, Bellingham WA, Chapters 4 -18, 1990.

[10] D. L. Fried, "Limiting Resolution Looking Down Through the Atmosphere," *Journal of the Optical Society of America*, Vol. 56, no. 10, pp. 1380-1384, Oct. 1966.

[11] F. Lei, and H. J. Tiziani, "Atmospheric Influence on Image Quality of Airborne Photographs," *Optical Engineering*, Vol. 32, no. 9, pp. 2271-2280, Sept. 1993.

[12] R. R. Beland, "Propagation Through Atmospheric Optical Turbulence, " *Atmospheric Propagation of Radiation*, F. G. Smith Ed., Information Analysis Center and SPIE Optical Engineering Press, Bellingham WA, Vol. 2, pp. 157-232, 1993.

[13] E. L. O'Neill, "Transfer Function for an Annular Aperture", *Journal of the Optical Society of America*, Vol. 46, no. 4, pp. 285-288, Apr. 1956.

[14] W. J. Smith, *Modern Optical Engineering*, McGraw-Hill, pp. 57-85, 1990.

[15] Private Communication Perkin-Elmer.

[16] W. L. McCracken, "Infrared Line Scanning Systems, " *Passive Electro-Optical Systems*, S. B. Campana Ed., Information Analysis Center and SPIE Optical Engineering Press, Bellingham WA, Vol. 5, p. 80, 1993.

[17] L. Schumann, and T. S. Lomheim, "Modulation Transfer Function and Quantum Efficiency at Long Wavelength in Linear Charge Coupled Imagers," *Applied Optics*, Vol. 28, no. 9, pp. 1701-1709, May 1989.

[18] J. F. Johnson, "Modeling Imager Deterministic and Statistical Modulation Transfer Functions," *Applied Optics*, Vol. 32, no. 32, pp. 6503-6513, Nov. 1993.

[19] D. H. Seib, "Carrier Diffusion of Modulation Transfer Function is Charge Coupled Imagers," *IEEE Trans. Electron Dev.*, Vol. 21, no. 3, pp. 210-216, March 1974.

---

[20] M. H. Crowell, and E. F. Labuda, "The Silicon Diode Array Camera Tube," *The Bell System Technical Journal*, pp. 1481-1528, May-June 1969.

[21] E. G. Stevens, "An Analytical, Aperture, and Two-Layer Carrier Diffusion MTF and Quantum Efficiency Model for Solid-State Image Sensor," *IEEE Trans. Electron Dev.*, Vol. 41, no. 10, pp. 1753-1760, October 1994.

[22] J. L. Harris, "Image Evaluation and Restoration," *Journal of the Optical Society of America*, Vol. 56, no. 5, pp. 569-574, May 1966.

[23] C. W. Barnes, "Object Restoration in a Diffraction-Limited Imaging System," *Journal of the Optical Society of America*, Vol. 56, no. 5, pp. 575-578, May 1966.

[24] A. V. Oppenheim, R. W. Schafer, *Digital Signal Processing*, Prentice-Hall, 1975.

[25] R. Barakat, "Application of the Sampling Theorem to Optical Diffraction Theory," *Journal of the Optical Society of America*, Vol. 54, no. 7, pp. 920-930, July 1964.

[26] J. L. Harris, "Diffraction and Resolving Power," *Journal of the Optical Society of America*, Vol. 54, no. 7, pp. 931-936, July 1964.

[27] F. O. Huck, N. Halyo, and S. K. Park, "Aliasing and Blurring in 2-D Imagery," *Applied Optics*, Vol. 9, no. 13, 2174-2181.

[28] E. A. Watson, R. A. Muse, and F. P. Blommel, "Aliasing and Blurring in Microscanned Imagery," *SPIE Infrared Imaging Systems*, Vol. 1689, pp. 242-250, 1992.

[29] J. W. Goodman, "Some Fundamental Properties of Speckle," *J. Opt. Soc. Am.*, vol. 66, no. 11, pp. 1145-1150, Nov. 1976.

[30] D. L. Fried, "Statistics of the Laser Cross Section of a Randomly Rough Target," *J. Opt. Soc. Am.*, vol. 66, no. 11, pp. 1150-1160, Nov. 1976.

[31] M. Francon, *Laser Speckle and Applications in Optics*, Academic Press, 1979.

[32] H. Fujii, T Asakura, Y. Shindo, "Measurement of Surface Roughness Properties by Using Image Speckle Contrast," *J. Opt. Soc. Am.*, vol. 66, no. 11, pp. 1217-1222, Nov. 1976.

[33] T. S. McKechnie, *Laser Speckle and Related Phenomena: Speckle Reduction*, Edited by J. C. Dainty, Springer-Verlag, vol. 9, pp. 123-170, 1975

[34] H. M. Pederson, "Theory of Speckle Dependence on Surface Roughness," *J. Opt. Soc. Am.*, vol. 66, no. 11, pp. 1204-1210, Nov. 1976.

[35] J. W. Goodman, "Some Effects of Target-Induced Scintillation on Optical Radar Performance," *Proc. IEEE*, vol. 53, no. 11, pp. 1688-1700, Nov. 1965.

[36] A. V. Jelalian, *Laser Radar Systems*, Artech House, pp. 6-10, 1992.

[37] B. J. Cooke, B. E. Laubscher, and C. C. Borel, "Methodology for Rapid Infrared Multi-Spectral, Electro-Optical Imaging System Performance and Synthesis," *Proc. SPIE Infrared Imaging Systems: Design, Analysis, Modeling, and Testing VII*, Orlando FL, pp. 52-86, April, 1996.

[38] F. X. Kneizys et al., "Users Guide To LOWTRAN 7," AFGL-TR-88-0177, 1988.

---

[39] T. S. Lomheim and J. F. Johnson, The Aerospace Corporation, MS-M4-980, P.O. Box 92957, Los Angeles, California 90009-2957.

[40] J. Vampola, *Readout Electronics For Infrared Sensors*, *The IR Electro-Optical Systems Handbook*, Vol. 3, SPIE Press, Bellingham WA, 1993.

[41] C. D. Motchenbacher, J. A. Connelly, *Low-Noise Electronic System Design*, John Wiley & Sons, 1993.

[42] S. M. Sze, *Physics of Semiconductor Devices*, John Wiley & Sons, 1981.

[43] R. K. Willardson, A.C. Beers, Editors, *Semiconductor and Semimetals: Volume 18, Mercury Cadmium Telluride*, Academic Press, 1981.

[44] J. Minkoff, *Signals, Noise, & Active Sensors*, John Wiley & Sons, 1985.

[45] Bradly J. Cooke, Mark Schmitt, Roy M. Goeller, Steve Czuchlewski, Kenneth Fuller, Nicholas Olivas, Bryan Laubscher and Robert Sander, "$CO_2$ DIAL Transmitter/Receiver Noise Characterization and Related Correlated Noise Issues," *Proc. SPIE, Gas and Chemical Lasers*, pp. 2-15, Feb. 1996.

[46] Special issue on fluctuation phenomena in electronic and photonic devices, *IEEE Trans. Elect. Dev.*, Vol. 41(11), pp. 1889-2222, November 1994.

[47] N. Menyuk, D. K. Killinger, and C. R. Menyuk, "Error reduction in laser remote sensing: Combined effects of cross correlation and signal averaging," *Applied Optics*, Vol. 24(1), January 1985.

[48] M. S. Keshner, "1/f noise," *Proc. of the IEEE*, Vol. 70(3), pp. 212-218, March 1982.

[49] F. N. Hooge, "1/f noise," *Physica*, Vol. 83B, pp. 14-23, 1976.

[50] S. D. Briles, Los Alamos National Laboratory, NIS-3, MS-D440.